

## Report on MEMS propulsion solutions



Team WhatdoyouMEMs

P. Code	Surname	Name
11071875	Bacconnier	Marc
10761124	Carminati	Matteo
10805938	Chianese	Elena Maria
10790352	Cocomazzi	Marco
10767560	Colombo	Andrea
10773170	Coppola	Riccardo
10766366	Corbo	Nicolò
10766052	Donati	Filippo
11093867	Pezzi	Francesco

## Space Propulsion Workshop

Prof: F. Maggi

L. Dossi, L. Caffiero

*M.Sc Space Engineering  
Academic Year 2024-2025  
Submission date: 09/04/2025*

**Abstract**

The miniaturization of space propulsion systems is a critical aspect to further enable operational capability of nanosatellites. This report investigates Micro-Electro-Mechanical Systems (MEMs) propulsion technologies as viable solutions for CubeSats requiring low Delta-V missions. Focusing on a 3U CubeSat, we perform an analysis of multiple MEMs propulsion configurations which are: solid propellant, vapor expansion, cold gas, and bipropellant systems. For each technology, we present a nominal design, assess power and volume requirements, and evaluate uncertainties in system performance, particularly those stemming from nozzle geometry. The analysis includes Monte Carlo simulations to study the sensitivity of thrust profiles to geometric uncertainties. The results are compared to identify the most promising propulsion solution for low thrust, short duration in space manoeuvres. This study supports the selection of optimized MEMs propulsion strategies for future CubeSat missions.

## Contents

<b>1</b>	<b>Introduction &amp; literature review</b>	<b>1</b>
1.1	MEMS materials and manufacturing techniques . . . . .	1
1.1.1	Materials . . . . .	1
1.1.2	DRIE . . . . .	1
1.1.3	Femtosecond laser machining . . . . .	1
1.1.4	Micro EDM . . . . .	1
1.1.5	Wafer bonding . . . . .	1
1.2	Overview of state of the art MEMS propulsion technology . . . . .	1
1.2.1	Solid propellant thrusters . . . . .	2
1.2.2	Vapor expansion thrusters . . . . .	2
1.2.3	Cold gas thrusters . . . . .	2
1.2.4	Liquid propulsion . . . . .	2
1.3	Common features . . . . .	2
1.3.1	Micro nozzle . . . . .	2
1.3.2	Plenum . . . . .	3
<b>2</b>	<b>Solid propellant</b>	<b>3</b>
2.1	Assumptions . . . . .	3
2.2	Design parameters . . . . .	3
2.2.1	Fuel . . . . .	3
2.2.2	Chosen parameters . . . . .	4
2.3	Nominal design modeling . . . . .	4
2.3.1	2D loss . . . . .	6
2.3.2	Architecture . . . . .	6
2.4	Nominal design results . . . . .	7
2.5	Power . . . . .	7
2.6	Monte Carlo analysis . . . . .	7
<b>3</b>	<b>Cold gas propellant</b>	<b>8</b>
3.1	Assumptions . . . . .	8
3.2	Design parameters . . . . .	9
3.3	Nominal design model . . . . .	9
3.3.1	Nozzle design . . . . .	9
3.3.2	Pressures in the system . . . . .	10
3.3.3	Masses and volumes of the system . . . . .	11
3.3.4	Architecture description . . . . .	11
3.4	Nominal design results . . . . .	11
3.5	Power . . . . .	12
3.6	Monte Carlo analysis . . . . .	12
3.6.1	Analysis results . . . . .	13
3.6.2	Minimum Impulse Bit (MIB) . . . . .	13
<b>4</b>	<b>Liquid vapor propellant</b>	<b>14</b>
4.1	Design strategy . . . . .	14
4.2	Assumptions . . . . .	14
4.3	Design parameters . . . . .	15
4.3.1	General architecture . . . . .	15
4.3.2	Water properties . . . . .	15
4.3.3	Chamber dimensions and heat transfer . . . . .	16
4.3.4	Iterative design degrees of freedom . . . . .	16
4.4	Nominal design model . . . . .	17
4.5	Nominal design results . . . . .	20
4.5.1	Results analysis . . . . .	20
4.6	Power requirements . . . . .	20

4.7 Monte Carlo analysis . . . . .	20
4.7.1 Uncertainties and Algorithm . . . . .	20
4.7.2 Results . . . . .	21
<b>5 Bi-propellant thruster</b>	<b>22</b>
5.1 Assumptions . . . . .	22
5.2 Design parameters . . . . .	22
5.2.1 Fuel and oxidizer . . . . .	22
5.2.2 Chosen parameters . . . . .	22
5.3 Nominal design model . . . . .	23
5.3.1 Nozzle design and performances . . . . .	23
5.3.2 Chamber and injector plate design . . . . .	23
5.3.3 Volume sizing . . . . .	24
5.3.4 Pressure cascade . . . . .	25
5.4 Nominal design results . . . . .	25
5.4.1 Architecture . . . . .	26
5.5 Power . . . . .	26
5.6 Monte Carlo analysis . . . . .	26
5.6.1 Minimum Impulse Bit . . . . .	27
<b>6 Results and conclusions</b>	<b>28</b>
6.1 Results . . . . .	28
6.2 Conclusion . . . . .	28
<b>A Authorship Declaration</b>	<b>33</b>

## 1 Introduction & literature review

The aim of this report is to showcase various micro-propulsion solutions exploiting MEMS manufacturing technologies, and to assess, through a preliminary study the ability of 4 selected systems to provide a valid propulsive solution for a 3U cubesat of mass  $6\text{ kg}$ , with a nominal Thrust of  $5\text{ mN}$  and nominal total  $\Delta v$  of  $0.5\text{ m/s}$ .

### 1.1 MEMS materials and manufacturing techniques

A brief rundown of the most used material and manufacturing techniques employed to produce MEMS for micro-propulsion are presented. Production of miniaturized valves and pumps were demonstrated in the past, as well as the possibility to integrate metallic elements into the design [1].

#### 1.1.1 Materials

MEMS systems are normally produced using pure Silicon as a base, its derivatives like silicon carbide (*SiC*) or other semiconductors, like germanium [2][3]. Additionally, for space propulsion application, more specifically in the field of Liquid Vaporizing Engines, ceramic substrate solutions are being explored [4][5].

#### 1.1.2 DRIE

The most employed manufacturing technique in MEMS system is the Deep Reactive Ion Etching (DRIE) that allows deep and narrow features to be etched into a Silicon Wafer. As a first step, a photoresist layer is deposited above the silicon substrate. Then, using Photolithography techniques, the pattern of the desired structure is transferred over it. This happens by exposing a selected part of the resists layer to UV light through a mask, in order to degrade it and remove it. The now exposed substrate is then exposed to the etching process, being blasted with a high-energy ion SF<sub>6</sub> beam that chemically etch it isotopically. Then a thin layer of a polymer based on CF<sub>4</sub>, is applied in a phase called pacification to protect the edges of the wedge, and then the process is repeated. This allows to generate features that are remarkably deep inside the Silicon wafer[6][7].

To further improve the flexibility of this method and enlarging the number of shapes that can be produced, a nest masking techniques can be applied, allowing to etch, in the same layer, features with different depth [7].

An advantage of this technique is that it is widely used in the general semiconductor industry so machines dedicated to it are easily available on the market pushing down the price of production. This also has problems, as the beam can etch only in the direction perpendicular to the wafer direction. This makes it impossible to produce axisymmetrical nozzles.

#### 1.1.3 Femtosecond laser machining

Micro features are generated by ablating the surface of the wafer using highly concentrated laser with a working time in the order of the Femtoseconds. This gives the opportunity to produce structures as small as  $1\text{ }\mu\text{m}$ . This technology can be applied to produce nozzles with diameters as low as  $30\text{ }\mu\text{m}$  as demonstrated in [8]. While promising results were obtained experimental data showed large off-axis thrust components due to miss-alignment in the nozzle axis.[8]

#### 1.1.4 Micro EDM

Micro Electrical Discharge Machining by discharging from an electrode a high number of electrons, generates an high temperature Plasma that locally melts the target material, carving the desired feature. For its nature, the material being machined needs to exhibit an high enough conductivity, limiting the choice to only metals and semi-conductors. While this method isn't bounded to produce features with rectangular cross-sections like the one described in 1.1.2, but the overall performance is hindered as this kind of processing produces slopes that are less smooth than the one obtained through other methods. Additionally this method can't produce structures smaller than  $10\text{ }\mu\text{m}$  [9].

#### 1.1.5 Wafer bonding

To generate more complex geometries, multilayer techniques are employed. The overall design is divided and etched onto multiple layers of silicon wafer that are then bonded together chemically. This gives the opportunity to build much more complex systems. [7]

## 1.2 Overview of state of the art MEMS propulsion technology

Due to the rising demand for this kind of solutions, the space industry is developing new kind of propulsive systems.

### 1.2.1 Solid propellant thrusters

Solid propellant Thrusters are generally composed of a small chip of solid propellant, with a small igniter, normally in the form of a resistance, and a nozzle. The disadvantages of these devices are the lack of control after ignition and that they are not able to restart. The reduced dimension of the system guarantees the possibility to fit multiple thrusters on the same board, providing the possibility to have multiple firing [10], however, the overall efficiency of the system tends to be pretty low, around 10 % [11].

### 1.2.2 Vapor expansion thrusters

Another possible configuration is the vapour expansion, consisting in the vaporization of a liquid inside a chamber using electric heating and then accelerating it through a nozzle to produce thrust. Various propellants can be employed, but water is mostly used as it constitutes a valid non-toxic option. This comes with some advantages such as the highest  $\Delta v$  per unit volume among all green propellants. [12]

Low pressure Micro-resistor jet designs, operating in the transient flow regime, were also proposed and analyzed using statistical analysis, and although promising, issues with the selections of the propellant and its storage prevented the actual commercialization of any product. [13][14]

### 1.2.3 Cold gas thrusters

This kind of thruster exploits propellant stored under pressure and accelerated through a nozzle to high velocity to produce thrusts. The technology maturation for this system is already pretty advanced, with some vendors already offering miniaturised flight proven off the shelves solutions for CubeSat, like GomSpace NanoProp, or the cold gas thruster developed by VACCO for *MarCO* mission [15][6]. Future developments will entail the development of even smaller system taking full advantage of MEMS technology to produce nozzles. Some studies in this regard was demonstrated in [8]

### 1.2.4 Liquid propulsion

Most solutions are monopropellant and exploit a catalyzation bed to decompose. While solutions based on Hydrazine[16], its high toxicity and therefore the costs associated with its usage makes it not compatible with low costs applications that are normally associated with CubeSat development[6]. Other solutions based on Hydrogen Peroxide decomposition into H<sub>2</sub>O and O<sub>2</sub>, and constitute a much greener and less expensive option, but at the same time, due to the fact that organic matter can act as a catalyst, and the generally long waiting time for launch for CubeSat might result in the loss of a big part of a large portion of the propellant before launch [17][6].

Bi-propellant solution offers the most powerful but at the same time most complex solution being developed for micro-propulsion units. Different design choices were explored over the years, with some older models proposing to use micro turbo pumps to drive the flow of propellants to the chamber, while more modern approaches use pressure feed systems, either employing self-pressurising or pressure regulated systems. This second approach results in simpler systems, but requires heavier masses to house the gas pressuriser.

Due to the high complexity of the deisgn and relative high costs incompatible with a cubesat development environment, bipropellant solutions remains, to date largelly unexplored, with some proposed design being developed by the *Massachusetts Institute of Technology* [18][7][19]. Is it also noted that new fesability studied were recently conducted by the Univrsity of Bologna, but the overall progress is still lacking [20]

## 1.3 Common features

### 1.3.1 Micro nozzle

Although each technology has each own characteristics, many aspect can be considered common. One of this is the nozzle as an expansion is beneficial for every each of them. The team considered a single design for the nozzle, considering the convergent angle  $\alpha = 45$  and divergent angle  $\beta = 15$  which was choosen from literature analysys. This choice imposes a common low  $\beta$  angle to minimize boundary layer in the divergent segment of the nozzle. From literature analysis the team considered it one of the biggest problems of micro noozles. For each configuration, once the expansion ratio was known, the performed iterative computation to recover the pressure ratio:

$$\frac{1}{\varepsilon} = \left( \frac{\gamma+1}{2} \right)^{\frac{1}{\gamma-1}} P_{ratio}^{\frac{1}{\gamma}} \sqrt{\frac{\gamma+1}{\gamma-1} \left( 1 - P_{ratio}^{\frac{\gamma-1}{\gamma}} \right)} \quad (1)$$

The nozzles' efficiency is evaluated through Eq. 2.

$$\eta = \frac{c_{T_{real}}}{c_{T_{ideal}}} \quad (2)$$

To determine this value, experimental results would be required, which is obtained through practical experiments or prolonged simulations. In our case, however, we do not possess such real parameters, so the efficiency cannot be determined exactly. But we may assume that the efficiency will be very low. Performance results in this report are based on a series of simplifying assumptions that will have a tendency to overestimate the capabilities of the system relative to real-world application. Also, as discussed in the literature [21], the efficiency of MEMs tends to be low due to their rectangular cross-sections, existence of strong boundary layer effects, large measurement uncertainty at small sizes, and limited application of assumptions commonly used in larger propulsion systems.

### 1.3.2 Plenum

For many applications in space propulsion, even for larger satellites than CubeSats, in addition to the tank another small volume containing propellant, is present: the plenum. Its function is to slow down the propellant before injection in order to convert dynamic pressure into static pressure. Usually, the plenum contains the propellant in vapor phase, ready for use. The team recognized that plenum must be able to conserve propellant in vapor phase in order to maintain a quasi equilibrium condition just close to utilization of the propellant itself. This implies that the plenum must be as little as possible, to reduce occupied space, but big enough to maintain equilibrium condition for any mass flow rate achievable by the engine. As little data were retrieved about plenum sizing the team considered direct proportions with respect to the tank and/or chamber, considering architecture design.

## 2 Solid propellant

In the context of this wide analysis regarding MEMs propulsion systems innovative solution, great interest should be reserved to solid propellant microthrusters (SPM) thanks to recent advancements in microfabrication techniques and small-scale theoretical understanding. SPM provide advantages of simple structure, high reliability, no frictional forces inherent to moving parts, no leakage of propellant and high propellant stability. SPM represent the possibility to minimize design's complexity. For example if compared to liquid and bi-propellant fuels they present a higher energy density and provide more throttle control, so in this design we can discard valves, pressurized storage tanks, and pumps that are not easily incorporated into such small devices. The major disadvantages are its low specific impulse and the one-shot use, which can be mitigated by adopting an array of multiple microthrusters as it will be chosen for our design. [22][6]

### 2.1 Assumptions

In order to keep the problem simple the following assumptions were considered.

- Calorically perfect gas.
- No 2-phase flow.
- Adiabatic walls.
- Neglection of thermal management.
- Isentropic nozzle expansion.
- Neglection of igniter.
- Constant burning area.
- Cilindrical grains.

### 2.2 Design parameters

As illustrated in the previous chapter, all designs should start from the same main requirements. For our design it was decided to develop an array of multiple micro-thrusters with isoentropic convergent-divergent conical micro-nozzles with circular section that will be subsequently quantified according to propellant length found in literature.

#### 2.2.1 Fuel

A composite propellant of ammonium perchlorate AP (as oxidizer) and HTPB (as polymer binder) was selected for the thrusters thanks to its high energy density. Aluminum was selected as metal fuel to add in the composite because of its ability to increase specific impulse despite the fact that it combusts in the gas-phase at very high temperatures.

	<b>Value</b>	<b>Unit</b>
$a$	1.55	$mm/(sbar^n)$
$n$	0.52	—
$\rho$	1670	$kg/m^3$
$\gamma$	1.3	—
$M_m$	$21.08 \times 10^{-3}$	$kg/mol$

Table 1: Key parameters for AP/HTPB/Al solid propellant

So the solid propellant chosen is AP/HTPB/Al with a percentage composition of 68/14/18. [23][22] Drawing from the literature, we adopted the propellant's characterizing parameters found in Table 1.[23]

### 2.2.2 Chosen parameters

Aiming to fulfill requirements, starting parameters were deeply researched and then fixed from literature. For combustion chamber conditions, with AP/HTPB/Al propellant choice, a chamber temperature of 2357 K was selected [23] after several similar numeric references were found ([23],[24]) together with a chamber pressure of 0.1 MPa [25]. Concerning Mach number in combustion chamber, it was fixed at 0.2 in order to keep the chamber velocity as small as possible. Finally, for nominal design configuration an area ratio of 10 was chosen among values found in literature, typically ranging between 3.6 and 11.4. [26] Considering the chosen temperature the material selected was epoxy resin, which has a perfect heat insulation despite having a low strength. [24]

## 2.3 Nominal design modeling

Starting from the presented data, both derived from requirements and literature research, the nominal design was developed through the following steps:

1. Pressure ratio  $P_e/P_c$  was obtained from area ratio  $\varepsilon$  using Eq. 1 assuming an expansion model based on isentropic single-phase flow and using an iterative method based on an initial guess. Having combustion chamber pressure  $P_c$  as an input, exit pressure  $P_e$  was so computed.
2. Exit velocity was obtained from Eq. 3.

$$u_e = \sqrt{\frac{2\gamma}{\gamma-1} \frac{R}{M_m} T_c \left(1 - \left(\frac{P_e}{P_c}\right)^{\frac{\gamma-1}{\gamma}}\right)} \quad (3)$$

3. Characteristic velocity was obtained from Eq. 4.

$$c^* = \frac{\sqrt{\frac{T_c}{M_m} R}}{\sqrt{\gamma \left(\frac{2}{\gamma+1}\right)^{\frac{\gamma+1}{\gamma-1}}}} \quad (4)$$

4. Thrust coefficient was computed using Eq. 5 for not-optimal nozzle with the additional static contribution, keeping in mind that ambient pressure conditions is zero in-space operations.

$$c_T = \sqrt{\frac{2\gamma^2}{\gamma-1} \left(\frac{2}{\gamma+1}\right)^{\frac{\gamma+1}{\gamma-1}} \left[1 - \left(\frac{P_e}{P_c}\right)^{\frac{\gamma-1}{\gamma}}\right]} + \frac{(P_e - P_a)A_e}{P_c A_t} \quad (5)$$

5. Specific impulse was modeled as follows with  $c^*$  from Eq. 4 and  $c_T$  from Eq. 5.

$$I_s = \frac{c_T c^*}{g_0} \quad (6)$$

6. As for throat area ( $A_t$ ) and exit area ( $A_e$ ), once all previous quantities were computed, they were easily obtained together with their diameters using the following model, keeping in mind that nozzle section is circular as already identified.

$$At = \frac{T}{P_c c_T} \quad ; \quad A_e = \varepsilon A_t \quad ; \quad A = \pi \left( \frac{d}{2} \right)^2 \quad (7)$$

7. Mass flow rate was obtained from Eq. 8.

$$\dot{m} = \frac{T - P_e A_e}{u_e} \quad (8)$$

8. Initial nozzle area was computed as illustrated in Eq. 9 where  $M_c$  is Mach number in combustion chamber.

$$A_i = \frac{A_t}{M_c} \left( \frac{2}{\gamma + 1} \left( 1 + \frac{\gamma - 1}{2} M_c^2 \right) \right)^{\frac{\gamma + 1}{2(\gamma - 1)}} \quad (9)$$

9. Once all propulsion system's main parameters were obtained, we computed burning rate and burning area to characterize combustion. The latter was set equal to the combustion chamber area.

$$r_b = a (P_c)^n \quad ; \quad A_b = \frac{\dot{m}}{\rho r_b} \quad (10)$$

10. In order to obtain burning time we imposed linear momentum conservation of spacecraft and propellant system. The force acting on the spacecraft is the whole thrust, while on the propellant only the dynamic term is acting.

$$\frac{dQ}{dt} = T - \dot{m} u_e = \dot{m} u_e + P_e A_c - \dot{m} u_e \quad ; \quad \frac{dQ}{dt} = P_e A_e \quad (11)$$

We can assume the chamber pressure to be constant during the burn.

$$\int_0^{t_b} dQ dt = \int_0^{t_b} P_e A_e dt \implies Q(t_b) - Q(0) = P_e A_e t_b \quad (12)$$

Assuming a reference frame fixed to the spacecraft before the manoeuvre.

$$m_{sc} \Delta v - \dot{m} t_b u_e = P_e A_e t_b \quad (13)$$

11. Once burning time was obtained, web thickness was also computed, from which we can get the total propellant volume Eq. 14.

$$w_b = r_b t_b \quad ; \quad V_p = w_b A_b \quad (14)$$

12. As for nozzle architecture a convergent-divergent conical model was chosen. Both convergent and divergent angles were found in literature [26] and fixated at  $\beta = 45^\circ$  and  $\alpha = 15^\circ$ . Knowing main sections diameters, we computed the length of convergent and divergent parts as well as total nozzle's length to complete the design.

$$L_{conv} = \frac{d_{inlet} - d_t}{2 \tan(\alpha_{conv})} \quad (15)$$

$$L_{dv} = \frac{1}{2} \frac{(d_e - d_t)}{\tan(\alpha)} \quad (16)$$

$$L_{nozzle} = L_{cv} + L_{dv} \quad (17)$$

13. A complete review of literature has been performed in order to decide the number of nozzles [ $n_s$ ] suitable for our design, the choice was made considering similar nozzle dimensions. The constraint we have imposed is to have a chamber length of around 1 mm [25]. This length is evaluated considering a margin of 5% [27] on the propellant volume to leave free space for the combustion.
14. Through Eq. 18 [24] we set a lower boundary for the wall thickness of the chamber.

$$\delta_{min} = \frac{\varphi_c P_{max} d_c}{2.3 \sigma_c - \varphi_c d_c} \quad (18)$$

where  $\varphi_c$  is found in literature to be 1.2 [24],  $P_{max}$  is equal to the chamber pressure,  $d_c$  is the chamber diameter and  $[\sigma_c]$  is the allowable strength of the chosen material.

### 2.3.1 2D loss

The preliminary analysis carried out does not include any kind of loss. For simplicity, the only deviation from the previous design considered were the 2D loss due to the divergent part of the nozzle. Eq. 19 is used to derive the divergence loss factor, which is then used in Eq. 20 to evaluate the real thrust provided.

$$\lambda = \frac{1 + \cos(\alpha)}{2} \quad (19)$$

$$T = \lambda \dot{m} u_e + P_e A_e \quad (20)$$

The target thrust is no longer achieved. Therefore the same modeling approach as before was used, though, with a different nominal thrust value. This new value is obtained by solving for the condition established in Eq. 21, which is stating that the thrust considering the loss must be 5 mN. The original parameters  $P_c$ ,  $T_c$  and  $\varepsilon$  are kept the same, meaning that  $u_e$  and  $P_e$  will not change in the new design.

$$\lambda \dot{m}_{new} u_e + P_e A_{e,new} = 0.005; \quad (21)$$

We can write  $A_{e,new}$  using Eq. 7 and Eq. 7 and  $m_{new}$  using Eq. 8 in which we can substitute again  $A_{e,new}$ . The only unknown after substitution is  $T_{new}$ , which can be therefore isolated obtaining Eq. 22.

$$T_{new} = \frac{0.05}{\lambda - P_e \varepsilon \frac{1}{P_c c_T} (1 + \lambda)} \quad (22)$$

### 2.3.2 Architecture

Basing on the nominal geometrical features that were computed and reported in table 3, the solid rocket motor architecture is presented.

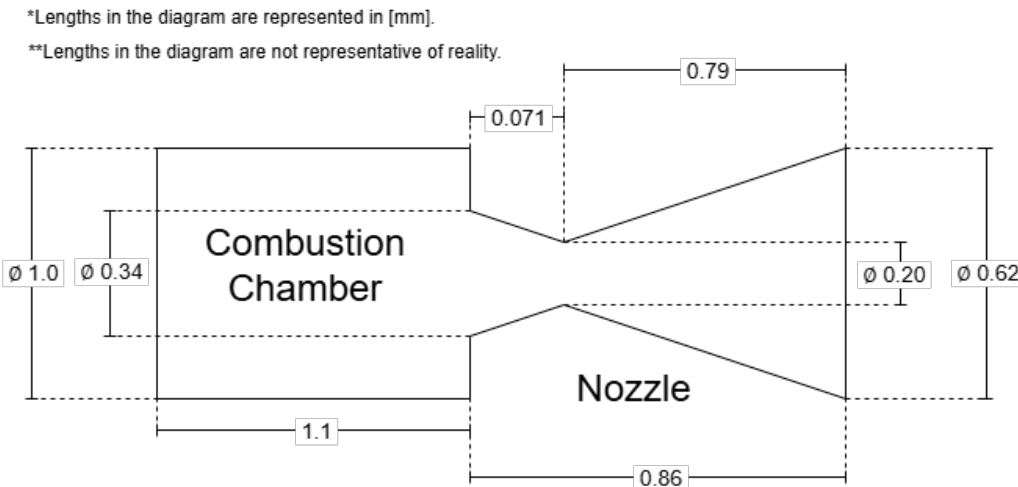


Figure 1: Schematic of the solid propulsion architecture

## 2.4 Nominal design results

The results obtained using the model described in the previous sections are all written in Table 2 and Table 3. The input thrust is the one described in Sec. 2.3.1.

	<b>Computed value</b>	<b>Unit</b>
$P_e$	955.17	Pa
$u_e$	2302.7	m/s
$c^*$	1445.0	m/s
$c_T$	1.6891	-
$\lambda$	0.9830	-
$T_{new}$	5.0817	mN
$\dot{m}$	2.0820	mg/S
$r_b$	1.5500	mm/s
$t_b$	666.67	ms
$M_p$	1.3880	mg
$\delta_{min}$	1.5365	μm
$T_{real}$	5.0000	mN
$I_s$	244.80	s
$I_v$	40882.1	kg s/m <sup>3</sup>
$I_{tot}$	3.3333	mNs

Table 2: Numerical results

	<b>Computed value</b>	<b>Unit</b>
$A_T$	0.0309	mm <sup>2</sup>
$A_e$	0.3085	mm <sup>2</sup>
$d_T$	195.72	μm
$d_e$	618.91	μm
$A_i$	0.0901	mm <sup>2</sup>
$d_i$	338.65	μm
$A_b$	0.8043	mm <sup>2</sup>
$d_b$	1011.98	μm
$w_b$	1033.33	μm
$V_p$	0.8311	mm <sup>3</sup>
$V_{cc}$	0.8727	mm <sup>3</sup>
$L_{cn}$	71.468	μm
$L_{dv}$	789.69	μm
$L_{nozzle}$	861.16	μm
$L_{cc}$	1102.7	μm

Table 3: Geometrical properties results

The values of volume and length are evaluated per single thruster, the number of thruster is set to 900 which consists of a 30x30 array. As expected the real thrust obtained considering losses is equal to the target one. All the values for the designed areas are feasible and possible to build in accordance with the data found in the literature [25] [26]. The burning rate is consistent with models present in the literature but considering the chamber pressure of 0.1 Mpa. As a consequence the total burning time is 655.95 ms, which means that for a single thruster burns for less than a millisecond. Consistent reference values for both the burning rate and the burning time for the AP/HTPB/Al propellant were found in [23]. The total length of the single thruster is around 2 mm, which is in the same order of magnitude of the current options studied on the literature. The length of the convergent is considerably smaller with respect to the divergent, but both are still coherent with nozzles found in previous studies [25]. It is relevant to note that the geometric features of the engine suffer from different kinds of uncertainties basing on the dimensions and on the manufacturing process. For example previous research [28] defined values of machining error for exit and throat sections of similar dimensions of 1.65% and 1.85%, respectively.

## 2.5 Power

Concerning power consumption, since as initial assumption it was chosen to neglect the igniter we can consequently assume 0 W as total power to run the unit.

## 2.6 Monte Carlo analysis

The Monte Carlo analysis was conducted to study thrust, ΔV and specific impulse behavior with respect to the uncertainties on the precision of the realization of a throat section of small dimensions and on parameters  $a$  and  $n$  of the Vieille's law. For all these parameters the team assumed a normal distribution, where standard deviation values are presented in table 4.

<b>Parameter</b>	<b>Standard deviation</b>
$a$	± 0.02 mm/(s·bar <sup>n</sup> )
$n$	± 0.01
$d_T$	± 2 %

Table 4: Uncertainties for the solid propulsion

Uncertainties for the Vieille's law parameters were set to values coherent with experimental results specific for AP/HTPB/Al

found in literature [3]. The uncertainty on the throat diameter is more hard to define, as it strictly depends on the manufacturing processes and on the nominal dimension. The value of machining error previously mentioned of 1.65% was extended to 2% to achieve a small margin. The Monte Carlo analysis was carried out for 63 samples of each parameter, leading to 250047 simulations. This number of simulations is sufficient to gain some insights on the behaviour of the motor, but it is important to note that a larger simulation would provide a more statistically complete set of data to study the behaviour of the output parameters.

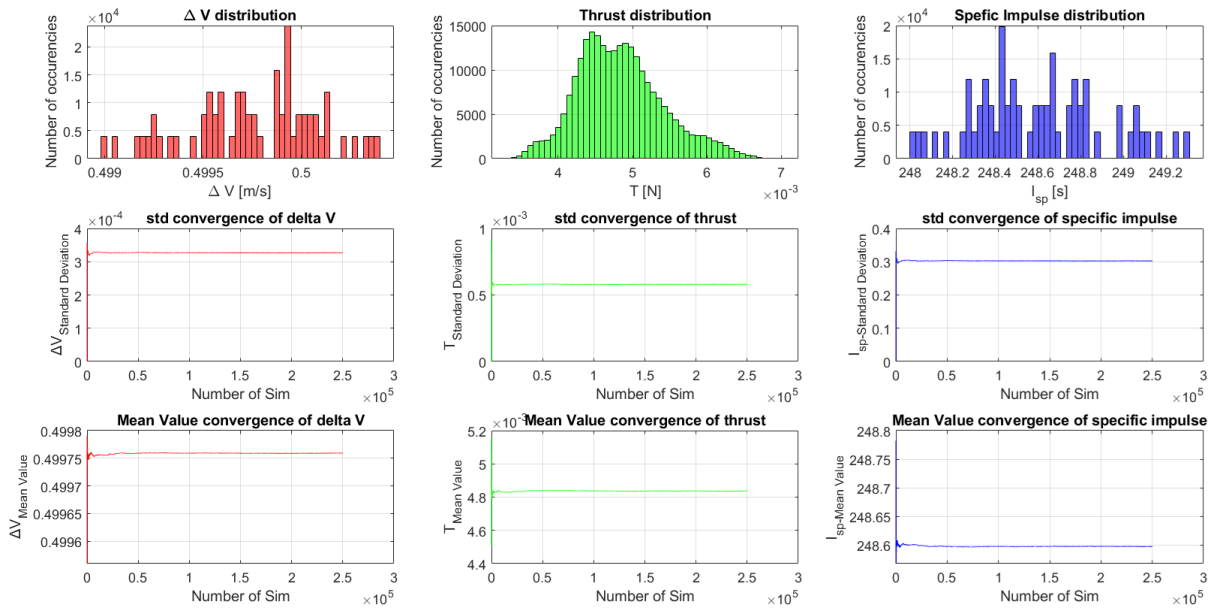


Figure 2: Results of Monte Carlo analysis

Results of the analysis overall demonstrate a good robustness of the solid rocket motor design. The  $\Delta V$  mean value quickly converges very close to the nominal 0.5 m/s, while the mean thrust converges slightly under the nominal value of 5 mN. This is in part due to statistical reasons, as larger simulations could potentially lead to more precise results. Nevertheless, the team presents the largest simulation that was conducted as the most significant for our discussion. The specific impulse converges as well to a mean value of around 248.6 s. Furthermore thrust assumes the closest distribution to a normal, while the specific impulse and  $\Delta V$  would need more simulations to achieve it, for the reasons previously mentioned.

### 3 Cold gas propellant

A cold gas thruster is a straightforward type of propulsion system that generates thrust by releasing a pressurized gas through a nozzle. It is called cold because, unlike conventional chemical propulsion systems, cold gas thrusters operate without combustion processes. They are therefore less efficient than monopropellant or bipropellant engines. However, their simple design (typically composed by pressurized gas tank, filter, pressure regulator, valve and nozzle) makes them more reliable and cost-effective. Cold gas thrusters are largely used for attitude control and manoeuvring.

#### 3.1 Assumptions

In order to model the system the following assumptions were considered:

- Calorically perfect gas.
- Isentropic flow from the exit convergent.
- Neglection of friction.
- Inlet under standard conditions.

### 3.2 Design parameters

The objective of this section is to describe the design process and to present the final results of the cold gas thruster sizing. The system requirements defined were based on the following inputs:

- Required thrust  $F = 5 \text{ mN}$
- Target  $\Delta V = 0.5 \text{ m/s}$
- Nitrogen-based expansion ( $N_2$ )

For the design process, different parameters were selected based on references in the literature [29]. The team identified a range of 1 to 4 bars common for cold gas thrusters. Thus an inlet of nozzle pressure  $P_{inlet}$  of 2 bars was selected. The temperature at the inlet was set to 300 K considering standard operational temperature of satellites, referring to 3.1. Finally, the expansion ratio and the nozzle's convergent and divergent half-angles were chosen as 15 ° based on recommendations from [29]. The complete set of input parameters is reported in Table 5.

Parameter	Symbol	Value	Unit
Expansion Ratio	$\epsilon$	15	-
nozzle Inlet Pressure	$P_{inlet}$	$2 \times 10^5$	Pa
Specific Heat Ratio	$\gamma$	1.4	-
Molar Mass of $N_2$	$M_{N_2}$	28.0134	kg/kmol
Gas Constant	$R_{gas}$	296.8	J/(kg K)
Inlet Temperature	$T_{inlet}$	300	K
Delta-V	$\Delta V$	0.5	m/s
Thrust	$T$	5	mN
Gravity Acceleration	$g_0$	9.81	m/s <sup>2</sup>
Spacecraft Mass	$m_{sc}$	6	kg
Convergent Half-Angle	$\alpha_{conv}$	15	deg
Divergent Half-Angle	$\alpha_{div}$	15	deg
Valve efficiency	$Y$	0.95	-

Table 5: Input parameters for cold gas thruster design

### 3.3 Nominal design model

#### 3.3.1 Nozzle design

The nozzle design starts by solving numerically Eq. 1 to obtain the pressure ratio  $P_{ratio}$  and thus the exit pressure  $P_e$ . Once  $P_{ratio}$  is obtained, the exit velocity is computed using Eq. 3

Considering the equations of mass flow rate  $\dot{m}$  and thrust  $T$ , it is possible to compute the throat area  $A_t$ , rearranging the two formulas, as function of known parameters. Considering the following equations:

$$\dot{m} = A_t P_{inlet} \gamma \frac{\sqrt{\left(\frac{2}{\gamma+1}\right)^{\frac{k+1}{k-1}}}}{\sqrt{\gamma R T_{inlet}}} \quad ; \quad T = \lambda \dot{m} u_e + A_e P_e \quad (23)$$

from which it is possible to obtain the throat area:

$$A_t = \frac{F / (\lambda u_e)}{\frac{\epsilon P_e}{\lambda u_e} + (P_{inlet} \gamma \sqrt{\left(\frac{2}{\gamma+1}\right)^{\frac{\gamma+1}{\gamma-1}}}) / \sqrt{\gamma R_{gas} T_c}} \quad (24)$$

And computing the exit area from Eq. 7 the respective diameters were retrieved:

$$d_t = \sqrt{\frac{4A_t}{\pi}} \quad ; \quad d_e = \sqrt{\frac{4A_e}{\pi}} \quad (25)$$

To compute the nozzle inlet area  $A_{inlet}$ , a laminar flow was assumed at the inlet. As no combustion is performed in a cold gas system, there is no need to purposely generate turbulence; instead, a laminar flow regime is preferable, as it minimizes pressure losses. The presence of the plenum can actually cover this functionality of reorganizing the flow other than recovering total pressure. For the same considerations, the team considered that the size of the valve and of the pipe connecting the plenum to the nozzle has the same dimension as the nozzle's inlet,  $A_{pipe} = A_{inlet}$ , minimizing turbulences. Thus, the team assumed a Mach number at the nozzle inlet  $M_{inlet} = 0.1$  and computed the Reynolds number, checking with Moody's diagram to be under laminar flow condition. In the  $A_{inlet}$

$$v_{inlet} = M_{inlet} * \sqrt{\gamma R T_{inlet}} \quad ; \quad Re_{inlet} = \frac{\rho_{inlet} v_{inlet} d_{inlet}}{\mu_{N_2}} \quad (26)$$

From these equations and Eq. 9, it is possible to compute the length of the nozzle from Eq. 15, Eq. 16, Eq. 17.

### 3.3.2 Pressures in the system

In this section the team retrieved the variation of pressure along the system.

The first assumption considered was about the density of the gas, which should vary along the pipe as pressure decreases. As the pressure loss is much lower than the nominal pressure, it is possible to assume that the correlated variation in density is negligible. Furthermore, considering continuity equation and the definition of pressure losses to demonstrate that:

$$\Delta P \propto \rho v^2 = \frac{\dot{m}^2}{\rho} \quad (27)$$

it follows that for a given mass flow rate, imposed by the chocking condition at the throat, the maximum pressure losses are obtained for the minimum density. In order to size the pressure losses for cold gas thrusters in this report it will be always considered the pressure downstream along all the regions of the subsystem.

Given the assumed pressure at the nozzle inlet  $P_{inlet}$ , the team evaluated the most significant pressure losses in order to compute the upstream pressure. The plenum and the nozzle were chosen to be as close as possible to maximize the recovery of total pressure from the plenum, with an ON/OFF valve after it to regulate the demand of thrust. Therefore, feeding line pressure losses were neglected but a valve pressure loss was considered.

Indeed, in the proposed architecture (see section 3.3.4), the valve is assumed to have the same diameter as the inlet of the nozzle. As a result, the valve was modeled as being directly connected to the plenum, and the pressure loss through the valve was treated similarly to an injection loss. This was interpreted as the pressure drop resulting from the gas transitioning from the larger plenum volume into the smaller valve cross-section leading towards the nozzle.

To estimate this loss, a discharge coefficient of  $C_d = 0.7$  and a compressibility factor  $Y = 0.95$  are considered. The choice of  $Y$  is based on [30], justified by the assumption of relatively low pressure losses and a very low  $\beta$  parameter, due to the plenum being much bigger.

$$\dot{m} = Y C_d A_{valve} \sqrt{2 \Delta P \rho_{inlet}} \quad (28)$$

$$\Delta P_{plenum \rightarrow nozzle} = \frac{1}{2 \rho_{inlet}} \left( \frac{\dot{m}}{Y C_d A_{inlet}} \right)^2 \quad ; \quad P_{plenum} = P_{inlet} + \Delta P_{plenum \rightarrow nozzle} \quad (29)$$

From the pressure in the plenum, assuming that the temperature  $T_{plenum}$  is equal to the one at inlet,  $T_{plenum} = T_{inlet}$ , it is possible to compute the density of the gas inside it:

$$\rho_{plenum} = \frac{P_{plenum}}{R_{N_2} T_{plenum}} \quad (30)$$

It is therefore possible to size the pressure at the exit of the regulator, assuming feeding line losses. It is worth noting that feeding line losses are being considered between the regulator and the plenum, assuming the regulator is as close as possible to the tank, right after the filter, to minimize pressure losses. This has been done as in a multiple thruster configuration, feeding lines for some of the thruster can reach relevant length, maybe up to more than half of 1U. For this reason, the feeding line length has been considered to be  $L_{feed} = 5 \text{ cm}$ . Computing the velocity in the pipe just by considering continuity equation:

$$v_{pipe} = \frac{\dot{m}}{\rho_{plenum} A_{pipe}} \quad ; \quad \Delta P_{regulator \rightarrow plenum} = \frac{1}{2} \rho_{plenum} v_{pipe}^2 f \frac{L_{feed}}{d_{pipe}} \quad (31)$$

$$P_{tank,f} = P_{regulator} = P_{plenum} + \Delta P_{regulator \rightarrow plenum} \quad (32)$$

In this way we can compute the pressure sensed by the regulator which will also be the final pressure of operations of the regulated pressure system.

### 3.3.3 Masses and volumes of the system

The required burn time and expelled propellant mass to achieve the required  $\Delta V$  are:

$$t_b = \frac{m_{sc} \Delta V}{F} ; M_{expelled} = \dot{m} t_b \quad (33)$$

By considering that at the start of operations the propellant will all be stored in the tank and the end of operations the remaining fuel in the tank will be at  $P_{tank,f}$ , always at the same temperature  $T_{tank} = T_{inlet}$  it is possible to compute:

$$M_{prop} = M_{expelled} + M_{tank,f} = \frac{P_{tank,i} V_{tank}}{R_{N_2} T_{tank}} = M_{expelled} + \frac{P_{tank,f} V_{tank}}{R_{N_2} T_{tank}} ; V_{tank} = \frac{M_{expelled} R_{N_2} T_{tank}}{P_{tank,i} - P_{tank,f}} \quad (34)$$

Due to a lack of precise data in the literature, the plenum volume  $V_{plenum}$  was assumed to be 1 % of the tank volume. From this consideration it is possible to compute the total volume of the system:

$$V_{TOT,CG} = V_{tank} + V_{plenum} + V_{nozzle} \approx V_{tank} \quad (35)$$

### 3.3.4 Architecture description

The architecture of the system selected for this case study is a simple configuration (Figure 3), incorporating the minimum number of components necessary to facilitate system sizing and computational analysis. While this model does not reflect all features of a real system of this size, it serves as a useful "first-order approximation" for understanding the fundamental principles of a cold gas thruster.

\*Lengths in the diagram are represented in [mm].  
\*\*Lengths in the diagram are not representative of reality.

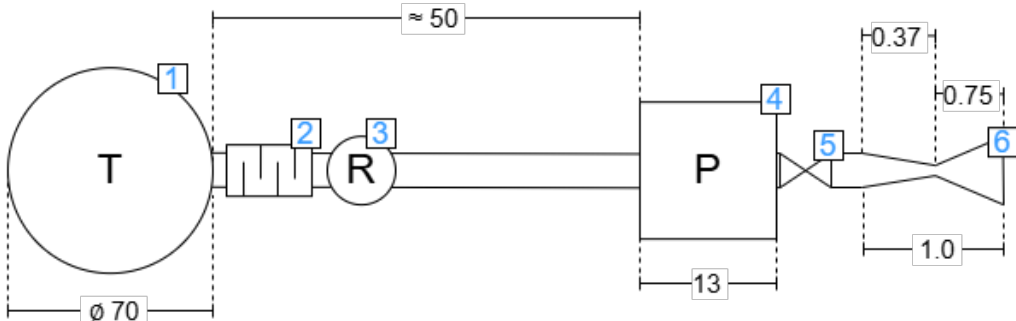


Figure 3: Schematic of the cold gas thruster architecture

The components constituting the system are respectively: a spherical storage tank 1; a particle filter 2 to remove impurities from the gas flow; a pressure regulator 3 that ensures a constant downstream pressure; a plenum chamber 4 to stabilize flow pressure before entering the nozzle; a ON/OFF valve 5 positioned at the plenum orifice, functioning as the injector; and finally, the nozzle 6, which accelerates the cold gas to generate thrust. The effect of the filet is actually only slightly changing the pressure of the tank, so for lack of validated data it was not modeled.

### 3.4 Nominal design results

The final design results obtained from the previous model are presented in the table 6.

Symbol	Value	Unit
$d_e$	540.00	$\mu\text{m}$
$d_{in}$	340.00	$\mu\text{m}$
$d_{throat}$	140.00	$\mu\text{m}$
$c^*$	435.78	m/s
$c_T$	1.65	-
$d_{tank}$	73.1	mm
$I_{sp}$	73.13	s
$L_{conv}$	370.00	$\mu\text{m}$
$L_{div}$	750.00	$\mu\text{m}$
$L_{nozzle}$	1110	$\mu\text{m}$
$\lambda$	0.983	-
$M_{expelled}$	$4.18 \times 10^{-3}$	kg
$\dot{m}$	$6.97 \times 10^{-6}$	kg/s

Symbol	Value	Unit
$P_e$	799.77	Pa
$P_{ratio}$	0.004	-
$P_{tank,i}$	$2.03 \times 10^6$	Pa
$P_{tank,f}$	$2.13 \times 10^5$	Pa
$r_{tank}$	36.6	mm
$t_b$	600	s
$t_{valve}$	0.001	s
$u_e$	703.26	m/s
$v_{injection}$	35.31	m/s
$V_{plenum}$	$2.05 \times 10^{-6}$	$\text{m}^3$
$V_{tank}$	$2.05 \times 10^{-4}$	$\text{m}^3$

Table 6: Cold gas design results

### 3.5 Power

The propulsion system requires electrical power mainly for the valve actuation. From literature [31] the team considered a valve consuming 0.2 W when closed and 5.2 W when open. This can actually seem an enormous power consumption for CubeSat, which usually generate around 2 W but the valve remains open for very small times.

### 3.6 Monte Carlo analysis

In this section is presented how the Montecarlo analysis for Cold gas thrusters was performed. The analysis consider uncertainties over two parameters relative to the nozzle: the throat diameter  $d_{throat}$  and the inlet diameter  $d_{inlet}$ . The team assumed manufacturing accuracy related to FLM (Femtosecond Laser Machining) processing, around  $\pm 2 \mu\text{m}$ , as mentioned in 1.1.3. The uncertainty was generated as a normal distribution around the nominal design value.

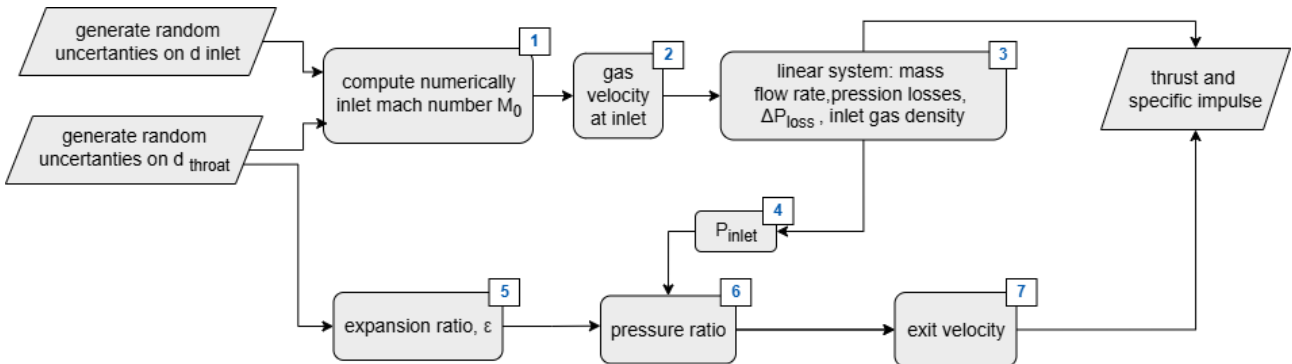


Figure 4: Flowchart of Monte Carlo algorithm

Description of steps presented in the flowchart:

1. Iterative computation of the Mach number at the inlet of the nozzle from Eq.9.
2. Once the Mach number is known, the velocity at the inlet is computed, assuming that the temperature is at standard condition:

$$v_{inlet} = M_{inlet} \sqrt{k R_{\text{gas}} T} \quad (36)$$

3. It is possible to compute three variables from the following non-linear system: the density at the nozzle inlet  $\rho_{inlet}$ , the pressure losses of the valve  $\Delta P_{plenum \rightarrow nozzle}$  and the mass flow rate  $\dot{m}$ :

$$\begin{cases} \dot{m} = Y C_d A_{\text{valve}} \sqrt{2 \Delta P \rho} \\ \dot{m} = \rho_{\text{injection}} A_{\text{inlet}} v_{\text{inlet}} \\ \Delta P_{\text{plenum} \rightarrow \text{nozzle}} = \frac{1}{2} \rho_{\text{injection}} \left( \frac{\dot{m}}{Y C_d A_{\text{inlet}}} \right)^2 \end{cases} \implies \begin{cases} \rho_{\text{inlet}} = \frac{A_{\text{throat}} P_{\text{plenum}} \Gamma}{A_{\text{inlet}} v_{\text{inlet}} + \frac{1}{2} A_{\text{throat}} \frac{v_{\text{inlet}}^2}{Y^2 C_d^2} \Gamma} \\ \Gamma = k \sqrt{\frac{\left(\frac{2}{k+1}\right)^{\frac{k+1}{k-1}}}{\sqrt{k R_{\text{gas}} T}}} \end{cases} \quad (37)$$

4. It is possible to recover the pressure at inlet of the nozzle with:

$$P_{\text{inlet}} = P_{\text{plenum}} - \Delta P_{\text{plenum} \rightarrow \text{nozzle}} \quad (38)$$

5. Since the geometry is computed, the expansion ratio is derived. Using Eq. 1

6. From the expansion ratio  $\epsilon$  it is possible to find the pressure ratio  $P_{\text{ratio}}$  and thus the exit pressure condition  $P_e$ .

7. The exit velocity can be retrieved as usual considering the pressure ratio in Eq. 3.

The outputs of this analysis are thrust and specific impulse, calculated using Eqs. 20 and 6:

### 3.6.1 Analysis results

As it possible to see in the figure 4 the mean values of the simulation results exhibit clear convergence toward the expected design value. In addition, the convergence of the standard deviations further demonstrates the correctness of the simulations.

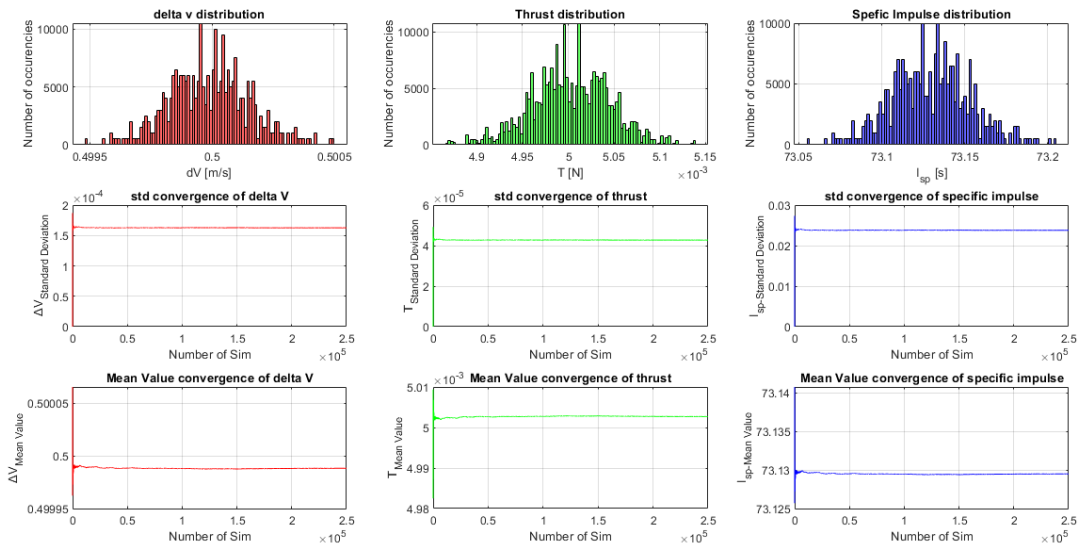


Figure 5: Monte Carlo simulation results

It is possible to note the small variation around the nominal design value. This result can shows the design robustness and the possible accuracy of this technology application.

### 3.6.2 Minimum Impulse Bit (MIB)

As cold gas thrusters are often used ADCS application Minimum impulse bit is a very important parameter both for Reaction Wheel de-saturation and for attitude control. For this kind of applications a very low MIB is targeted. For current state of technology for bigger satellites MIB values are usually in the range of  $(10^{-6}; 10^{-4}) [\text{N} \cdot \text{s}]$ . For small satellites cold gas thruster could possibly allow even small orbital maneuvers and maintenance.

The team computed the MIB considering constant thrust during the actuation time of a valve, retrieved from literature  $t_{valve} = 1\text{ ms}$  [31].

$$MIB = 2 \int_{t_0}^{t_0 + t_{valve}} T dt \approx 2T t_{valve} = 10^{-5} \quad (39)$$

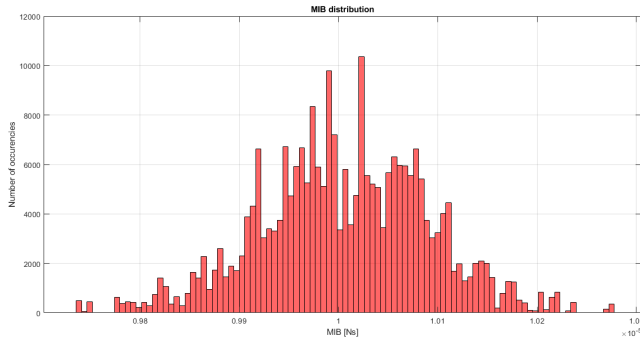


Figure 6: MIB distribution

## 4 Liquid vapor propellant

A potential alternative to conventional cold-gas propulsion—capable of overcoming the limitations imposed by the on-board propellant volume and system mass is resistive electric propulsion, and in particular, water evaporation-based VLM (Vaporizing Liquid Microthruster) technology. This approach relies on low-pressure liquid storage to reduce both mass and volume, with the propellant subsequently vaporized via thermal resistive heating. The application of this technology to MEMS systems is particularly compelling due to its excellent adaptability to miniaturized environments. If the goal is to achieve higher performance while minimizing system dimensions, the ability to store the propellant in liquid form, thereby significantly reducing volume, combined with the use of electrical energy to increase the enthalpy content of the flow, represents a major advantage. Moreover, the overall system architecture enables the recovery of residual heat from nearby electronic components, serving the dual purpose of cooling those elements while simultaneously supplying thermal energy to generate thrust.[32] [33]

### 4.1 Design strategy

An iterative strategy was adopted for the development of the engine design. The process began with the construction of a preliminary model of the main components, in which key parameters were defined based on data available in the scientific literature. A global simulation of engine behavior was then performed, primarily employing a top-down approach that follows the flow path through the system. This was followed by an optimization phase and a comparison with experimental data, aimed at assessing the consistency of the model and identifying both its limitations and strengths.

### 4.2 Assumptions

In order to simplify the creation, modeling, and analysis of the engine, several simplifying assumptions were introduced. Nevertheless, these assumptions do not significantly compromise the validity of the results or the objectives of this preliminary design phase.

Suggested
Standard Temperature in Tank
Calorically Perfect Gas
No Heating Power Dispersion
Chamber Friction Neglected
Isentropic Flow in Nozzle
Added
Incompressible liquid
No convective motion

Table 7: Modeling Assumption

The incompressible liquid assumption implies that density of the liquid phase remains constant, reasonable for low Mach number in liquid flow. Additionally, the model does not consider explicitly convective motions within the chamber. The vaporization process is considered as a "black-box" power transfer, where the liquid absorbs energy and transitions to vapor without internal flow dynamics being accounted for. It is important to note that the decision of not modeling convective motion is strong. However, despite this simplification, excellent results have been obtained, demonstrating good agreement with more detailed simulations. The reliability of these results will be presented and discussed in the following chapters.

### 4.3 Design parameters

#### 4.3.1 General architecture

\*Lengths in the diagram are represented in [mm].

\*\*Lengths in the diagram are not representative of reality.

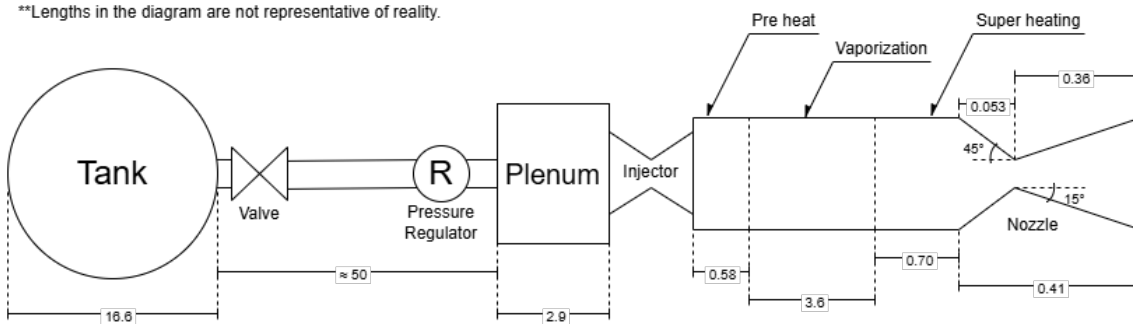


Figure 7: Schematic of the VLM architecture

#### 4.3.2 Water properties

Water was assigned as the propellant for our propulsion system. The advantages of its utilization are discussed in 1.3.2). Due to its thermophysical properties, water requires a specific modeling approach. We opted to treat the thermodynamic properties on a case-by-case basis, depending on the extent to which the assumption of constant values would influence the model's accuracy. Below, we list the parameters that were assumed to be constant along with the corresponding values; the resulting error introduced by these simplifications, compared to a more realistic model, is discussed in section 4.5.1.

Constant	$R$	$\gamma$	$\rho_{liq}$	$c_{liq}$	$c_{vap}$	$T_t^0$	$\mu_{liq}$
Value	461.5	1.33	997	4186	1864	298.15	0.00089
Unit	$J/(kg K)$	-	$kg/m^3$	$J/(kg K)$	$J/(kg K)$	K	$Pa S$

Table 8: Water properties

Three additional properties were instead modeled in greater detail, as they are expected to significantly influence the design of the vaporization chamber, which will be discussed in the following sections:

- **Vapor Density:** Modeled using the Ideal Gas Law, assuming dependence on the specific gas constant and on pressure and temperature:

$$\rho_v(T_v, P_v) = \frac{P_v}{R_{H_2O} T_v} \quad (40)$$

- **Vaporization Temperature and Latent Heat:** modeled through linear interpolation of thermodynamic tables [34], based on their dependence on pressure. Boiling occurs when the vapor pressure of a given liquid reaches the external pressure. The relationship between these parameters is governed by the Clausius–Clapeyron thermodynamic law. [35][36][37]:

$$T_{vap}(P_v, \Delta H_{vap}) = \left( \frac{1}{T_0} - \frac{R \ln(\frac{P_v}{P_0})}{\Delta H_{vap}} \right)^{-1} \quad (41)$$

#### 4.3.3 Chamber dimensions and heat transfer

While the main model of the Vaporization Chamber will be addressed later in 4.4, certain parameters must be defined from the outset in order to proceed with the analysis:

- **Two-dimensional sizing:** While the length is left as a parameter to be determined by the design process, the other two dimensions have been fixed based on real-case references, specifically [32]. We have chosen a structure with 9 micro-channels, each with dimensions of  $d_{ch} = 120 \times 80 \mu m$ , featuring heat exchange surfaces on the bottom and lateral sides, while the top surface provides structural integrity. The use of multiple channels instead of a single one results in a higher heat exchange area to volume ratio and helps to prevent potential convective or turbulent flow issues [38].
- **Maximum temperature:** based on an analysis of the operating regimes of the materials involved, primarily silicon and molybdenum derivatives. Silicon allows for lower operational temperatures but avoids oxidation risks, whereas molybdenum enables higher working temperatures. Our design employs a molybdenum film coating the main silicon structure, allowing for operating temperatures up to  $T_{max} = 850 ^\circ C$  without significant variation in resistive properties [39], [12], [1].
- **Maximum thermal power:** Given the difficulty in identifying a direct correlation between thrust and required power from available sources [40], we referred both to the relation presented in [33] and to statistical studies on electrical systems in 3U CubeSats [41], establishing a value of  $\dot{Q}_{max} = 15 W$ .
- **Thermal power input per unit length:** To model the heat transfer within the vaporization chamber using a constant heat input per unit length approach, we relied on the data obtained so far. By dividing the maximum thermal power previously established by the length scale derived from the model in [32], we identified the value of  $Q/L = 2500 \frac{W}{m}$  as a reliable estimate.

The need to choose a reference power per unit length and the other two dimensions was essential to derive a reasonable chamber dimension. Other approaches to dimensioning the chamber were tested, such as using a parameter similar to characteristic length  $L^*$  (in this case referred to proper length needed for vaporization and heating) and its usage for retrieving the chamber volume, but this parameter is absent in the literature.

#### 4.3.4 Iterative design degrees of freedom

In order to proceed with the global modeling and simulation of the system, and in line with the iterative approach, the degrees of freedom for the optimization problem were defined. As initial values, those used in real-case examples from the aforementioned literature were adopted: [32]

Inputs		
Heating Power $\dot{Q}$	Tank Pressure $P_t$	Tank Exit Velocity $u_e$
Tank Volume $V$	Mass Flow Rate $\dot{m}$	Exit Area $A_e$

Table 9: VLM DoFs

As introduced, these parameters are iterated in order to find the most suitable configuration for the respecting of imposed requirements.

#### 4.4 Nominal design model

The nominal design is presented in the following lines:

1. **Tank:** The occupied volume is modeled by assuming a perfectly spherical structure, along with the maximum activation time of the thruster, based on the known parameters of the exit flow.

$$r_t = \sqrt[3]{\frac{3}{4} \frac{V}{\pi}} \quad t_b = \frac{V}{\dot{m}} \frac{1}{\rho_l} \quad (42)$$

2. **Valve:** the pressure losses are modeled as concentrate according to:

$$\Delta P_v = \frac{1}{2} \rho_l u_f^2 K_v \quad (43)$$

where  $K_v = 10$  is the loss coefficient. No direct value was found for this parameter and for this kind of small configuration, so it has been set with respect to bigger (but still miniaturized and similar) valves.

3. **Feeding lines:** modeled as channels where the flow occurs under laminar regime, resulting in a distributed pressure loss. The radius is affected by the flow velocity as a consequence of the continuity equation, which in turn influences the friction factor. The model requires a check on the Reynolds number in the lines to verify the validity of the hypothesis used for the friction factor computation:

$$r_f = \sqrt{\frac{\dot{m}}{\rho_l u_t} \frac{1}{\pi}} \quad \Rightarrow \quad \Delta P_f = \frac{1}{2} \rho_l u_t^2 f \frac{L_f}{2 r_f} = \frac{1}{2} \rho_l u_t^2 \frac{64}{Re} \frac{L_f}{2 r_f} = u_t \frac{16 \mu L_f}{r_f^2} \quad (44)$$

The flow velocity has been verified in computations to ensure that the fluid remains within the incompressible flow regime.

4. **Plenum and Injector:** The plenum was selected as a percentage of the chamber volume, ensuring a constant pressure upstream of the chamber. About the injector, its losses were considered as 15% of the combustion chamber. This percentage was used to retrieve the injection area and velocity:

$$\Delta P_j = \%_j P_c \quad \Rightarrow \quad A_j = \frac{\dot{m}}{C_d \sqrt{2 \frac{\Delta P_j}{\rho_l}}} \quad \Rightarrow \quad u_j = u_t \frac{A_f}{A_j} \quad (45)$$

5. **Vaporizing chamber:** Modeled as a three-zone heat exchanger with constant heat flux, the initial and final sections are not treated as micro-channels but rather approximated as lumped areas to allow the computation of the nozzle's geometric parameters. In general, moving along it towards the nozzle, the evolution of the flow is as follows:

- **Inlet Section:** Depending on the dimensions of the chamber (also considered in this case as a lumped area without micro-channels), the flow velocity varies accordingly:

$$u_c = u_j \frac{A_j}{A_c} \quad (46)$$

- **Heating Zone:** Modeled as a constant-pressure duct in which the fluid absorbs enthalpy up to the vaporization temperature, calculated based on the inlet properties of the chamber. The amount of absorbed enthalpy will consequently determine the length of this region:

$$T_{vap} = f_1(P_c) \quad \Rightarrow \quad \dot{Q}_r = \dot{m} c_l (T_{vap} - T_j) \quad \Rightarrow \quad L_r = \frac{\dot{Q}_r}{\dot{Q}_{/L}} \quad (47)$$

The absence of pressure losses in this region is related to no friction hypothesis.

- Evaporation Zone: Modeled as a constant-pressure and constant-temperature duct (as expected for phase change) in which the fluid absorbs the latent enthalpy required for vaporization, calculated based on the inlet properties of the chamber. This enthalpy will, in turn, determine the length of this region:

$$l_{lat} = f_2(P_c) \quad \Rightarrow \quad \dot{Q}_{vap} = l_{vap} \dot{m} \quad \Rightarrow \quad L_{vap} = \frac{\dot{Q}_{vap}}{\dot{Q}_{/L}} \quad (48)$$

The interface between the two phases will experience a sudden increase in flow velocity within the duct, due to the drastic decrease in density, calculable through the ideal gas law, as a direct consequence of the continuity equation:

$$\rho_v = \frac{P_c}{RT_{vap}} \quad \Rightarrow \quad u_v = u_c \frac{\rho_l}{\rho_v} \quad \Rightarrow \quad P_{0v}, T_{0v}, Ma_v \quad (49)$$

During the modeling the inlet velocity has been a critical parameter in order to avoid the excessive increasing of the velocity and Mach number. This problem will be better discussed in results part.

- Superheating Zone: Modeled as a duct governed by Rayleigh flow, with length and heat absorption derived from the preceding zones. The outlet properties are computed as follows:

- Calculation of the thermodynamic property ratios at the beginning of the Superheating Zone with respect to choking conditions, performed through linear interpolation of thermodynamic tables [42]:

$$T_{0v}, P_{0v}, Ma_v \quad \Rightarrow \quad \frac{T_{0v}}{T_0^*} = g_1(Ma_v) \quad \frac{P_{0v}}{P_0^*} = g_2(Ma_v) \quad (50)$$

- Calculation of the temperature at the outlet of the combustion chamber by converting the thermal power of the heat exchange over the remaining length of the chamber:

$$\dot{Q}_s = \dot{Q} - \dot{Q}_r - \dot{Q}_{lat} \quad \Rightarrow \quad T_{0ec} = T_{0v} + \frac{\dot{Q}_s}{\dot{m} c_v} \quad (51)$$

where "ec" refers to the exit of the chamber.

- Calculation of the total temperature ratio between the inlet and outlet of the combustion chamber. Comparing this value with the critical ratio corresponding to Mach equal to 1 (from Rayleigh tables) allows to verify that sonic velocity has not been reached within the chamber:

$$Ma_{ec} = 1 \quad \leftrightarrow \quad \frac{T_{0v}}{T_0^*} > \frac{T_{0v}}{T_{0ec}} \quad (52)$$

- Calculation of the Mach number at the combustion chamber exit, reusable for determining the pressure ratio and subsequently the total pressure at the exit:

$$Ma_n = g_1^{-1} \left( \frac{T_{0ec}}{T_0^*} \right) \quad \Rightarrow \quad \frac{P_{0ec}}{P_0^*} = g_2(Ma_{ec}) \quad (53)$$

where the inverse function means that table entries are processed in reverse order.

6. **Nozzle:** Modeled as a conical converging-diverging nozzle (see 1.3.1), traversed by an isentropic flow with sonic conditions at the throat section, where the main geometric properties can be identified, such as the throat area and the lengths of the various sections:

$$A_t = \frac{\dot{m}}{\Gamma P_{0n}} \quad \Rightarrow \quad L_{conv} = \frac{r_c - r_t}{\tan(\beta)} \quad \Rightarrow \quad L_{div} = \frac{r_e - r_t}{\tan(\alpha)} \quad (54)$$

where the first formula is the one that guarantees chocking condition in the throat [43]. Additionally, all parameters required for performance evaluation are computed, such as exit pressure, expansion ratio, and finally the thrust coefficient.

$$\epsilon = \frac{A_e}{A_t} \quad \Rightarrow \quad P_e = h_1(\gamma, P_{0n}, \epsilon) [1] \quad \Rightarrow \quad C_t = h_2(\gamma, P_{0n}, P_e, \epsilon) [5] \quad (55)$$

7. **Performance:** Following the acceleration of the flow, the engine is capable of producing thrust, which can be quantified based on the obtained data, along with the maximum achievable  $\Delta v$  for this propulsion architecture. As previously discussed (see 2.3.1), the expansion in the nozzle introduces performance losses that must be accounted for in the computation of performance parameters:

$$T = \lambda P_{0n} A_t C_t \quad \Delta v = \frac{T}{M_{sc}} t_b \quad (56)$$

Furthermore, knowing the opening and closing time of the valve used in the system, it is possible to compute the Minimum Impulse Bit (MIB), the sensitivity of the propulsion system, defined as the minimum impulse it is capable of delivering:

$$MIB = 2t_v T \quad (57)$$

8. **Total dimensions:** Having defined all geometric parameters, it is possible to compute the total length and volume occupied by the propulsion system. For this modeling, any electrical/electronic subsystems required are neglected, and the analysis is limited to the sum of the volumes and lengths of the individual components, excluding the dimensions of the valve, regulator, and injector. The nozzle volume is calculated as the sum of the volumes of two truncated cones, whose bases correspond to the inlet, throat, and exit areas:

$$L_{tot} = r_t + L_p + L_f + L_c + L_{nc} + L_{nd} \quad V_{tot} = V_t + V_p + A_f L_f + A_c L_c + V_{nc} + V_{nd} \quad (58)$$

9. **Analysis and iteration:** Once the engine simulations has been completed, it is analyzed together with the geometric parameters and iteratively modified in pursuit of improved optimization and robustness. The process involves computing the engine performance within a neighborhood for each of the six degrees of freedom, in order to identify relationships between the parameters and their effects on overall performance. After selecting a single parameter for modification, the cycle is repeated until the nominal design is finalized. The objectives at the time of the iteration are the following:

- Power Consumption Minimization: Given the significant impact of the thermo-resistive system on the overall power budget, minimizing energy consumption is of primary importance.
- System Volume Minimization: One of the main advantages of MEMS technology lies in miniaturization; thus, exceeding size constraints would undermine this key strength and must be avoided.
- Uncertainties Robustness maximization: Due to the potential uncertainties introduced by material processing at such small scales, it is essential to avoid extreme design solutions that may prove impractical in real-world applications.
- Gravimetric Specific Impulse Maximization: As the principal parameter for assessing the efficiency of the propulsion system relative to the propellant mass, maximizing this value is critical to enable reduced water loading and minimize both mass and volume.
- Maximum Chamber Temperature and Nozzle Inlet Mach verification: During the design process, these two primary constraints were introduced to prevent material degradation, as melting or efficiency loss in the resistive behaviors, and to limit total pressure losses in the convergent section of the nozzle.

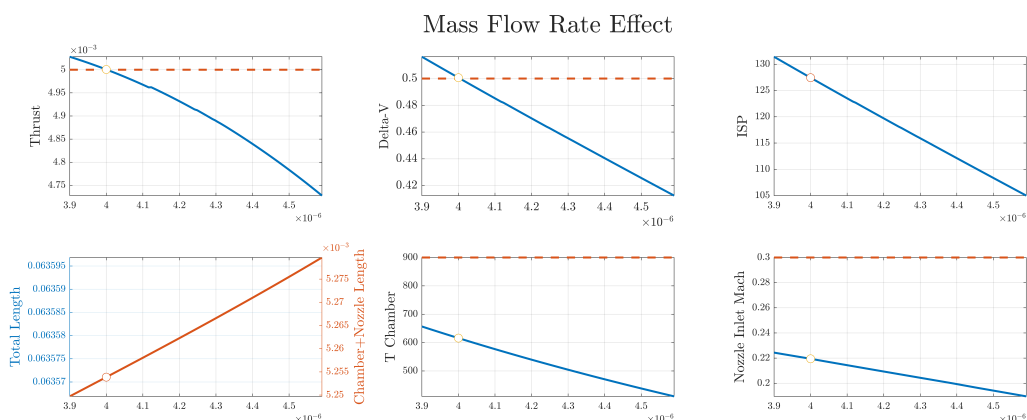


Figure 8: Optimization Process Example

## 4.5 Nominal design results

The following results are based on the following choice of DoF:

$\dot{Q} = 12.1 \text{ W}$	$P_t = 2.6 \text{ bar}$	$u_t = 0.5 \text{ m/s}$
$V = 2.41 \text{ cm}^3$	$\dot{m} = 4 \text{ mg/s}$	$A_e = 0.1 \text{ mm}^2$

Table 10: Fixed Parameters

	Computed value	Unit
$t_b$	600.7	s
$u_c$	0.0697	m/s
$T_{vap}$	384.3823	K
$l_{vap}$	2226	kJ/kg
$P_c$	1.5	bar
$\rho_v$	0.8459	kg/m <sup>3</sup>
$\text{Ma}_v$	0.1690	-
$T_{0n}$	620.7	K
$P_{0n}$	1.511	bar
$\text{Ma}_n$	0.2195	-
$\epsilon$	4.75	-
$C_t$	1.598	-
$P_e$	3406	Pa
$T$	5.0005	mN
$I_{sp}$	127.43	s
$\Delta v$	0.5006	m/s
$MIB$	0.01	Ns

Table 11: Numerical results

	Computed value	Unit
$A_t$	0.021	mm <sup>2</sup>
$A_c$	0.0576	mm <sup>2</sup>
$A_f$	0.00802	mm <sup>2</sup>
$L_c$	4.8	mm
$L_n$	0.413	mm
$V_p$	0.241	cm <sup>3</sup>
$L_{tot}$	6.36	cm
$r_t$	8.3	mm
$V_{tot}$	2.435	cm <sup>3</sup>

Table 12: Geometrical properties results

### 4.5.1 Results analysis

Based on these results, several observations on requirements, constraints and assumption can be made:

- The requirements are met precisely in the nominal configuration, with accuracy up to the fourth significant figure.
- The calculated values are consistent with those reported in the literature for comparable cases [44]
- The constraints imposed on temperature and inlet velocity to the nozzle are satisfied with a considerable margin. The assumptions of ideal behavior for the thermal exchange material and isentropic nozzle flow do not introduce significant deviations from the real-case scenario.
- The modeling of temperature and latent heat of vaporization may introduce a potential error, when compared to constant standard-condition values, of 2.87% and 1.4% respectively. [40]

## 4.6 Power requirements

An analysis of the electrical power requirements reveals that the vast majority of the energy is consumed by the vaporization chamber and its associated resistive heating system. The only other component with a non-negligible power demand is the valve, whose behavior is assumed as previously described in Section 3.5.

## 4.7 Monte Carlo analysis

### 4.7.1 Uncertainties and Algorithm

As previously discussed for other cases, it is necessary to perform a Monte Carlo analysis to assess the impact of uncertainties both manufacturing and power related on the nominal performance of the system. Three parameters were selected for this analysis: two geometric (the nozzle throat diameter and the injector diameter), and one thermal (the transmitted heating power). The uncertainty values found in the literature are as follows:

- Geometric Uncertainties: These refer to the percentage error on the nominal diameter based on real MEMS manufacturing cases. [28] The error was interpreted as a  $3\sigma$  confidence interval, which allowed for the computation of the variance of the normal distribution associated with each parameter.
- Power Uncertainties: This refers to the absolute error on the current and voltage supplied to the system. [45] A 6V system architecture was assumed. The associated uncertainties were propagated through the power calculation, and the resulting power uncertainty was then treated as a  $3\sigma$  confidence interval.

Parameters	Mean Value	Standard Deviation
Nozzle Throat Diameter	0.16373 mm	1.0915 $\mu$ m
Injection Diameter	0.90696 mm	4.9883 $\mu$ m
Heating Power	12.1 W	0.0105 W

Table 13: VLM Uncertainties

The simulation model differs significantly from the one used in the design phase. In fact, uncertainties on the throat area imply that, in order to verify sonic conditions at the throat, the mass flow rate must be adjusted accordingly. However, the governing relation, reported below, is highly implicit, as the total properties themselves are functions of the mass flow rate:

$$A_t = \frac{\dot{m}}{\frac{\Gamma P_{0n}(\dot{m})}{\sqrt{R T_{0n}(\dot{m})}}} \quad (59)$$

As a result, the computational model requires an iterative solution of the propulsion system. An initial estimate of the mass flow rate (starting with the nominal value) is provided, and a top-down simulation is performed. The computed throat area is then compared with the input value. If the discrepancy exceeds a defined tolerance ( $10^{-10}$ ), the mass flow rate is updated using the residual and the simulation is restarted. On the other hand the other two parameters do not require modifications to the simulation structure, except for the fact that the geometric dimensions, rather than being unknowns, are treated as fixed input parameters in the model.

#### 4.7.2 Results

The key output parameters for engine validation are once again the Minimum Impulse Bit, Delta-V, Thrust, and Specific Impulse. The corresponding results are presented below:

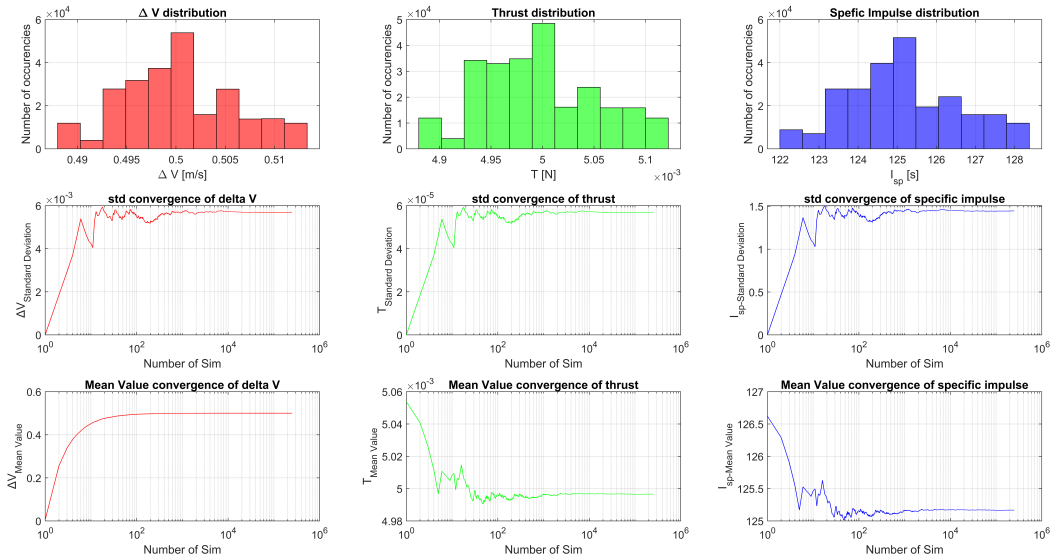


Figure 9: VLM Monte Carlo Analysis

It can be observed that the distribution of the obtained values resembles a normal distribution, although it does not follow it precisely.

This outcome deviates slightly from expectations, and the following hypothesis has been formulated: the number of simulations performed (250,000) was not sufficient for the distribution to fully converge to a normal shape. Nevertheless, a strong convergence is still achieved for both the mean and standard deviation values (represented here in a semi-logarithmic scale on the x-axis). Overall, the design demonstrates robustness and resilience under non-ideal conditions, though it exhibits a slightly lower mean thrust compared to the requirement (4.99658 mN), while delivering a higher-than-expected Delta-V (0.50023 m/s). The Minimum Impulse Bit value, being directly derived from the thrust in each simulation, results in an average slightly below the nominal but remains consistently comparable (0.099932 Ns).

## 5 Bi-propellant thruster

Among various types of MEMs thrusters presented, little interest is given to bipropellant solutions. While liquid bipropellant typically offer higher thrust and higher specific impulse when thrust levels are above 1 N, several challenges are encountered at lower thrust levels. Notably injector criticalities occur due to difficulty in handling such a small flow rate. Other problems arise from propellant mixing, which can be hard to control since orifices tend to plug. Furthermore compared to the miniaturization of other kind of thrusters, bipropellant shows lower reliability and poor pulse performances.

### 5.1 Assumptions

In order to keep the problem simple the following assumptions were considered.

- Neglection of friction
- Calorically perfect gas
- No heat dispersion
- Isentropic flow from the exit convergent

### 5.2 Design parameters

Together with the main parameters and requirements of the study highlighted in subsection (1.-), several additional design parameters were deeply researched and fixed to complete the design. It was chosen to develop a pressure-fed system with helium ( $H_e$ ) as pressurizing gas, stored in two pressurizing tanks. The reasons behind this choice are mass and volume constraints of the satellite, that prevent us from implementing a turbo-fed system, and the high value of hydrazine vaporization temperature, which discourages the possibility of a self-pressurized system choice. [20] The system architecture consists of two independent pressure regulators and two valves, together with fuel and oxidizer tanks and two plenums used to stabilize pressure and mitigate fluctuations in the combustion chamber. An isentropic convergent-divergent conical nozzle with circular section was selected for the configuration.

#### 5.2.1 Fuel and oxidizer

The selected propellant consists of hypergolic couple with Hydrazine ( $N_2H_4$ ) as fuel and Nitrogen Tetroxide ( $N_2O_4$ ) as oxidizer. So we have a chemical reaction where two substances ignite spontaneously upon contact with each other, without needing any external ignition source.

	<b>Value</b>	<b>Unit</b>
$O/F$ ratio ( $r_{O/F}$ )	1.08	-
$\rho$	1200	$kg/m^3$
$\mathfrak{M}$	19.5	$kg/kmol$
$\gamma$	1.26	-

	<b>Fuel</b>	<b>Oxidizer</b>	<b>Unit</b>
$\rho$	1447	1003.7	$kg/m^3$
$\mu$	0.913	0.33	$C_p$

Table 15: Fuel and oxidizer parameters

Table 14: Mixture parameters

In literature theoretical chamber performances for combinations of liquid rocket propellants are available [43]. The values used for the propulsion system model are presented in Table 14 and Table 15.

#### 5.2.2 Chosen parameters

For combustion chamber conditions a pressure of 0.1 MPa was selected, this choice is not-compliant with literature, where values found are higher [7], but is justified by the low thrust requirement. Among values of expansion ratios, usually ranging between 3.6 and 11.4 in literature [26], we selected a value of 10. For contraction ratio the value was found and fixed at 50 [19]. Concerning characteristic length, main literature values found range between 0.76-0.88 m

[46], but the design value was finally fixed at 0.2 m because of miniaturization incompatibility with the original values, a literature reference was found to justify this choice. [18]

### 5.3 Nominal design model

Starting from the parameters discussed in Sec. 5.2, a complete sizing of geometry and performances is conducted.

#### 5.3.1 Nozzle design and performances

The value of the expansion ratio is used to evaluate the pressure ratio through Eq. 1 using a solver due to the implicitness of the equation. Using the imposed chamber pressure and temperature, we can derive the exit pressure  $P_e$  of the nozzle and the exit velocity from Eq. 3. Furthermore the nozzle performance can now be easily analyzed by evaluating the thrust coefficient with Eq. 5. With the available data it's possible to design the whole geometry of the nozzle starting from the throat area  $A_t$  from Eq. 7 and the external area  $A_e$  from Eq. 7, while the entrance area  $A_c$ , which will coincide with the chamber area, is estimated from Eq. 60 which exploit the contraction ratio imposed for the design.

$$A_c = \epsilon_c A_t \quad (60)$$

Once nozzle's circular sections are computed we can retrieve all the diameters. With Eq. 15, Eq. 16 and Eq. 17 we can evaluate the nozzle length by selecting the convergent angle  $\beta$  and divergent angle  $\alpha$  from literature [26] resulting respectively in  $45^\circ$  and  $15^\circ$ .

#### 5.3.2 Chamber and injector plate design

The design of the chamber is done considering the characteristic length from which we can derive the volume using Eq. 61.

$$V_c = A_t L^* \quad (61)$$

Since the chamber area is already known the total chamber length is easily derived.

$$L_c = \frac{V_c}{A_c} \quad (62)$$

Chamber performances are evaluated through  $C^*$  with Eq. 4, from which we can also get  $I_s$  from Eq. 6. The total mass flow entering the chamber is computed from Eq. 20, while with Eq. 63 and Eq. 64 the mass flow for both fluids is evaluated. Total mass flow is considering also the 2D losses by introducing the parameter lambda taken from Eq. 19.

$$\dot{m}_f = \frac{\dot{m}}{1 + r_{O/F}} \quad (63)$$

$$\dot{m}_o = \dot{m}_f r_{O/F} \quad (64)$$

To design the injection plate the discharge coefficient  $C_D$  of orifices is needed, typically this value if found in tables associated to a diameter [43]. In the current design the orifice diameter chosen for fuel injector  $d_f$  is [7]  $1 \mu\text{m}$ , which is lower than the minimum value present in tables, therefore minimum  $C_D$  found is chosen 0.7. From the available data we can compute the total area needed to guarantee correct discharge of mass flow rate of fuel. Eq. 65 is used to define the total area needed to treat the fuel mass.

$$A_{F_{tot}} = \frac{\dot{m}_f}{C_D \sqrt{2 \Delta P_{inj} \rho_f}}; \quad (65)$$

This equation requires  $\Delta P_{inj}$ , which is taken from literature considering a like impinging doublet, resulting in 15% of  $P_c$ . The choice of like impinging is driven by the liquid state of both fluids and their storability, this will result in the same number of orifices for both. The obtain area value is divided by the single orifice area of the fuel to obtain the number of orifices needed  $N_o$ . With Eq. 65 we can derived also the total area for oxidizer flow, from which we can get both area  $A_o$  and diameter  $d_o$  of oxygen orifices since the number of orifices is the same of the fuel. Last analysis that needs to be conducted is the flow direction after impinging, we want that to be  $0^\circ$  with respect to horizontal direction. Imposing an angle for the oxidizer flow, which is set to be  $15^\circ$  [47] we can get the needed fuel flow angle with Eq. 66.

$$\gamma_f = \arcsin \left( \frac{u_o \dot{m}_o}{u_f \dot{m}_f} \sin(\gamma_o) \right) \quad (66)$$

where  $u_o$  and  $u_f$  are the exit velocities of the two fluids and are evaluated using Eq. 67.

$$u = C_D \sqrt{2\Delta P_{inj} \rho} \quad (67)$$

### 5.3.3 Volume sizing

In order to size fuel and oxidizer tanks, we start from the burning time computation through Eq. 11, achieved from the imposition of linear momentum conservation of spacecraft and propellant system. Once  $t_b$  is computed, having both fuel and oxidizer mass flow rates, we can evaluate fuel and oxidizer stored mass with Eq. 68 and Eq. 69. A 5% margin is added to mass values for redundancies [].

$$M_f = \dot{m}_f t_b (1 + 5\%); \quad (68)$$

$$M_o = \dot{m}_o t_b (1 + 5\%); \quad (69)$$

Having fuel and oxidizer mass and their density values, volume of the tanks can be easily obtained as in Eq. 70 and Eq. 71, where a 2% margin is included to prevent them from being completely filled.

$$V_{ft} = \frac{M_f}{\rho_f} (1 + 2\%) \quad (70)$$

$$V_{ot} = \frac{M_o}{\rho_o} (1 + 2\%) \quad (71)$$

Concerning shape, a spherical tank volume was assumed for both fuel and oxidizer storage and so diameters  $d_{ft}, d_{ot}$  can be easily evaluated from volumes.

Aiming to size the feeding lines, a total length  $L_{fl}$  of 10 cm is approximated on the basis of satellite's dimensions and a common range of diameter values  $d_{fl}$  is found in literature [7] and is so fixed at 30  $\mu m$ . Feeding lines section  $A_{fl}$  is then determined and used to compute flow velocity in feeding lines through Eq. 72 and Eq. 73.

$$u_f = \frac{\dot{m}_f}{A_{fl} \rho_f} \quad (72)$$

$$u_o = \frac{\dot{m}_o}{A_{fl} \rho_o} \quad (73)$$

In order to size the plenums several choices were made following the same reasoning explained in previous chapters (). It was decided to size both of them with the same volume, area and cuboid shape. Each plenum gives an additional volume contribute  $V_{pln}$  of 0.5% of tank volume and presents a section area that covers 10 times the combustion chamber area. Their length  $L_{pln}$  can be easily evaluated from volume and area described. Lastly, aiming to size the pressure-fed system with helium as pressurizing gas, two spherical tanks were designed. Temperature in pressurizing tanks was fixed at 298 K as standard value while pressure was found in literature [48] and fixed at 1.3 MPa. To evaluate the volume of the pressurizing tank we can impose the conservation of the mass of the gas between two instants of time, the start of the mission and the moment when the propellant is fully consumed. The density is evaluated using the law of perfect gas Eq. 74.

$$\rho_{g2} = \frac{P_{tank}}{T \frac{R}{M}} \quad (74)$$

where  $P_{tank}$  is the pressure in the propellant tanks which is evaluated through the pressure cascade technique explained in Sec. 5.3.4. With the same equation but using the pressure of the pressurizing tank we can get the density of the gas at the beginning of the mission  $\rho_{g1}$ . The Eq. 75 derives from the conservation of mass described above and it is used to get the volume of each pressurizing tank  $V_{pt}$ .

$$V_{pt} = V_{tank} \frac{\rho_{g1} - \rho_{g2}}{\rho_{g2}} \quad (75)$$

This procedure is performed for both oxidizer and fuel resulting in two different volumes for the pressurizing tank. Finally the total volume of the propulsion system  $V_{tot}$  is evaluated summing all different contributes.

### 5.3.4 Pressure cascade

Starting from combustion chamber pressure, Pressure Cascade technique is then used to obtain tank pressures by going backwards in the feeding lines until the propellant tank, through a series of intermediate static pressure stages as follows. The procedure is the same for the two different fluids, indeed it is presented in a general case. At first the pressure of the chamber rise of 15% due to injection losses as described before. Then as we enter the plenum the pressure will decrease due to the static pressure recover obtained by slowing down the flow. From the plenum to the valve friction losses are considered using Eq. 76 assuming half of the total feeding lines length.

$$\Delta P_{feeding} = \frac{1}{2} \rho v^2 f \frac{L_{fl}}{d_{fl}} \quad (76)$$

$d_{fl}$  is the diameter of the cable, fixed at  $30 \mu m$  as stated in Sec. 5.3.3, and  $f$  is obtained from the Moody diagram [43] evaluating the Reynolds parameter using and Eq. 77 where Eq. 72 and Eq. 73 are used for the velocity in the feeding lines.

$$R_e = \frac{\rho u D}{\mu} \quad (77)$$

The values of viscosity  $\mu$  can be found in Tab. 15. The pressure receive a little jump due to the valve which can be quantified using Eq. 78

$$\Delta P_{valve} = \frac{1}{2} \rho u^2 K_{valve} \quad (78)$$

The value of  $K_{valve}$  is a constant of the valve and was found in literature to be 0.55 [49]. The final value of the pressure tank is then evaluated by summing all contributes discussed above, obtaining two different values for oxidizer tank  $P_{ot}$  and fuel  $P_{ft}$ .

$$P_{tank} = P_c + \Delta P_{inj} + \Delta P_{valve} + \Delta P_{feeding} \quad (79)$$

## 5.4 Nominal design results

	Computed value	Unit
$P_e$	1064.4	Pa
$u_e$	2862.0	m/s
$c_T$	1.7089	-
$c^*$	1786.0	m/s
$\lambda$	0.9830	-
$\dot{m}$	1.6667	mg/s
$\dot{m}_f$	0.8013	mg/s
$\dot{m}_o$	0.8654	mg/s
$t_b$	590.40	s
$M_{ox}$	536.46	mg
$M_f$	496.42	mg
$N_O$	3.0000	-
$u_f$	7.8338	mm/s
$u_o$	12.197	mm/s
$P_{ot}$	0.1150	MPa
$P_{ft}$	0.1150	MPa
$I_s$	305.82	s
$I_v$	36698	kg s/m <sup>3</sup>
$I_{tot}$	2.9520	Ns

Table 16: Numerical results

	Computed value	Unit
$A_t$	0.0293	mm <sup>2</sup>
$A_e$	0.2926	mm <sup>2</sup>
$d_t$	193.01	$\mu m$
$d_e$	610.35	$\mu m$
$A_c$	1.4629	mm <sup>2</sup>
$d_c$	1364.8	$\mu m$
$V_c$	5.8517	mm <sup>3</sup>
$L_c$	4.0000	mm
$V_{ft}$	35.014	mm <sup>3</sup>
$V_{ot}$	54.517	mm <sup>3</sup>
$d_f$	10.000	$\mu m$
$d_o$	9.7783	$\mu m$
$V_{pl}$	1.7507	mm <sup>3</sup>
$A_{pl}$	14.629	mm <sup>2</sup>
$L_{pl}$	119.67	$\mu m$
$V_{ptf}$	360.79	mm <sup>3</sup>
$V_{pto}$	561.74	mm <sup>3</sup>
$L_{cn}$	585.89	$\mu m$
$L_{dv}$	778.77	$\mu m$
$L_{nozzle}$	1364.7	$\mu m$
$V_{tot}$	1014.4	mm <sup>3</sup>

Table 17: Geometrical properties results

It is also possible to underline how the specific impulse results to be higher than other configurations exploited in this report, as previously stated in the beginning of this chapter. The number of orifices is really small, but the value is justified by miniaturization typical dimensions. The unusual value that stands out in results' tables is the oxidizer's orifice diameter

which results to be smaller than the fuel's one. This can be explained by the fact that we are rounding up the number of orifices without changing fuel's orifices diameter, while instead the oxidizer orifices depend directly from this parameter. This will result in a fuel-rich mixture which is not a problem since mass flow rates of fuel and oxidizer are close enough. It is also important to check that total length and total volume are small enough to fit inside a 3U cube-sat, therefore they fulfill all requirements. All nozzle geometric parameters are feasible compared to usual MEMs nozzles found in literature [26].

#### 5.4.1 Architecture

\*Lengths in the diagram are represented in [mm].  
\*\*Lengths in the diagram are not representative of reality.

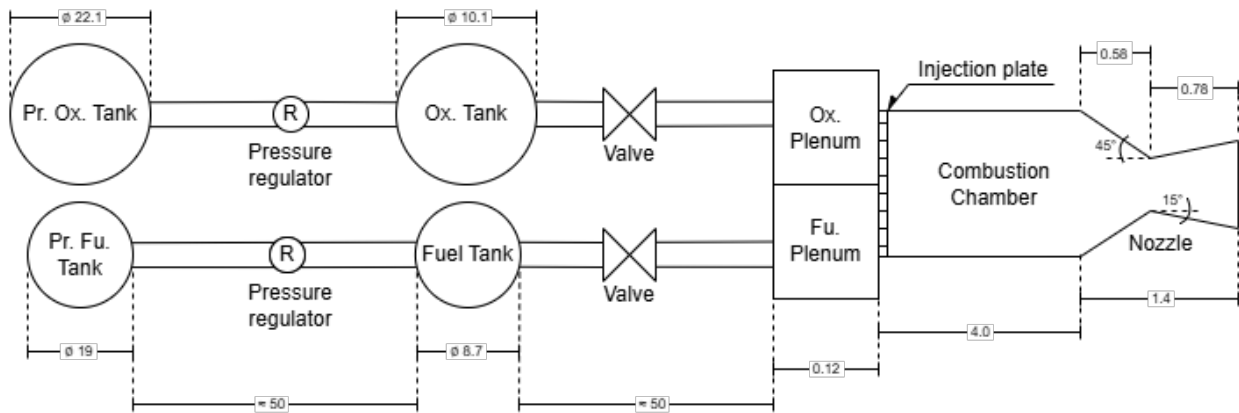


Figure 10: Bipropellant nominal architecture

#### 5.5 Power

Concerning the system's power consumption, the main element to take into account are the feeding valves. The other elements of the architecture do not consume any power, as the pressure regulators are mechanical parts and thanks to the hypergolic reaction in the combustion chamber there's no need of ignition. From literature it was possible to derive a value of the energy consumption  $E$  consisting in 116 mJ and the pulse  $t_v$  of 50 ms for valves in microthruster applications [50]. Therefore the total power consumption is 2.32 W, evaluated through Eq. 80.

$$P = 2 \frac{E}{t_v} \quad (80)$$

#### 5.6 Monte Carlo analysis

For the bipropellant Monte Carlo analysis, the team assumed constant plenum pressures, assuming ideal behavior of the pressure regulator.

Uncertainties were applied to two key parameters:

- The throat diameter of the nozzle,  $d_t$ . An uncertainty of  $\pm 2 \mu\text{m}$  has been retrieved from literature;
- The diameters of the orifices in the injector plates  $d_{\text{orifices,fuel}}$  and  $d_{\text{orifices,oxidizer}}$ . An uncertainty of  $\pm 1.68\%$  over the size of the orifice has been retrieved from literature;

It is important to note that for each simulation the two holes on each injection plate were assumed to have exactly the same dimensions. This is actually very far from reality as each hole should be modeled with its own dimension. The team agreed that this would increase too much the computational cost without actually affecting too much the results of the simulations, which are actually affected by the total area of the holes.

In order to model the variation of parameters in the chamber the team decided to solve a non linear system composed of Eqs. 23, and equations were added:

$$\dot{m} = \rho_{chamber} A_{chamber} u_{chamber} \quad (81)$$

$$\dot{m}_{oxidizer} = c_D A_{injections, oxidizer} \sqrt{2 \rho_{liquid, oxidizer} (P_{plenum, oxidizer} - P_{chamber})} \quad (82)$$

$$\dot{m}_{fuel} = c_D A_{injections, fuel} \sqrt{2 \rho_{liquid, fuel} (P_{plenum, fuel} - P_{chamber})} \quad (83)$$

$$\dot{m} = \dot{m}_o + \dot{m}_f \quad (84)$$

This system was solved by the use of MATLAB function *lsqnonlin* which approximate solution to a local minimum. As solution of nominal condition was for sure near design condition due to very low uncertainties, the convergence to solution is pretty fast and allowed the team to run thousands of simulations. In this way the team was able to compute the solution allowing variable chamber pressure  $P_{chamber}$ , chamber temperature  $T_{chamber}$ , propellant mass flow rate  $\dot{m}$ , oxidizer mass flow rate  $\dot{m}_{oxidizer}$ , fuel mass flow rate  $\dot{m}_{fuel}$ , computing for each simulation an approximation of the equilibrium condition in combustion chamber.

From these parameters the team recovered the performances of the engine for each simulation. Here are reported the results of the Montecarlo Analysis:

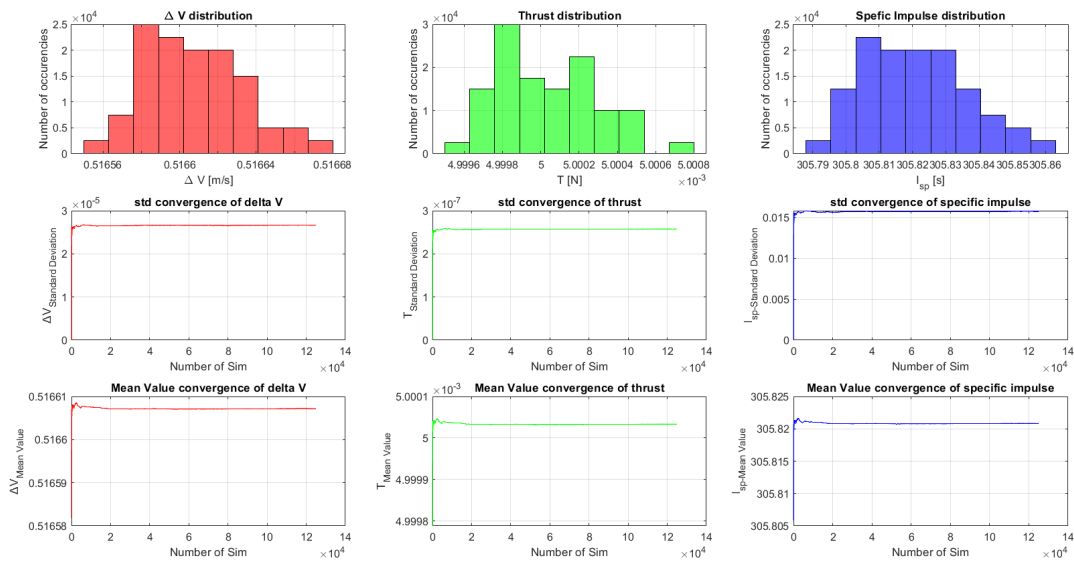


Figure 11: Montecarlo Analysis result

From the presented plots it is possible to see the convergence of the results of the Montecarlo, validating the results. It is furthermore possible to note improved mean performances over the  $\Delta V$  as a result of imposed margins over the mass. Both thrust and specific impulse instead don't have too significant variations with respect to nominal value, which could be a indicator of a solid design.

### 5.6.1 Minimum Impulse Bit

as already defined in the section 3.6.2, it is possible to define the Minimum Impulse Bit considering constant thrust. The team performed again the same analysis for the Bipropellant thrusters although usually this type of propellant systems consider throttability. By the architecture considered by the team there would be no possibility to control the mass flow nor the thrust. Thus the definition of MIB. For future developing different architecture could be designed

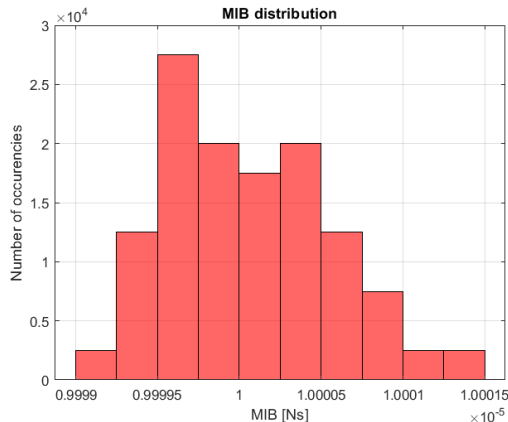


Figure 12: MIB analysis results

## 6 Results and conclusions

### 6.1 Results

	$V_{tank}$ [mm <sup>3</sup> ]	$L_{nozzle}$ [\mu m]	$\varepsilon$ [-]	$c_T$ [-]	$c^*$ [m/s]	$I_{s_{real}}$ [s]	$V_{chamber}$ [mm <sup>3</sup> ]	Power [W]
Solid	–	861.16	10	1.6891	1445.0	244.8	0.8727	0
Cold gas	205000	1110	15	1.65	435.78	73.13	–	0.2 - 5.2
VLM	2410	413	4.75	1.598	795.73	127.43	0.2765	12.1
Bipropellant	89.531	1364.7	10	1.7089	1786.0	305.82	5.8517	2.32

Table 18: Comparison of micro-propulsion technologies (transposed)

As expected, looking at the volume of the propellant tank for each configuration (except the solid, which don't need a tank), the cold gas which store a gas (lower density) has the highest tank volume. The VLM and the bipropellant that store liquid have way smaller tanks. The bipropellant, looking at the values is clearly more convenient to optimize the size, but it implies two tanks (oxidizer and fuel) which double the complexity and the number of potential failure of components.

The length of the nozzle is in the same order of magnitude for the solid, VLM and bipropellant configuration. Only the VLM is shorter than the others. The smaller the nozzle, the smaller would be the accuracy of manufacturing, increasing uncertainties and possible imperfection that could lead to fluid dynamics non-wanted behavior. Nonetheless, smaller length implies smaller expansion ratio.

Concerning the power consumption of the propulsion systems, solid propulsion is very convenient because it requires no power to perform. The cold gas and bipropellant demands on power seems manageable for a 3U CubeSat, even if not equipped with deployable solar panels (to enhance the total power available). However, the VLM requires a lot of power to heat the water. That amount of power might not be available for every CubeSat missions, especially the solar panels body-mounted only CubeSat.

For the  $I_s$ , the cold gas, as the simplest configuration and less efficient configuration. As the bipropellant, as the most complex configuration, is the most efficient configuration. The VLM appears as an evolution of the cold gas thruster (more efficient) but implies more complexity and power. The solid configuration is more efficient compared to the cold gas and VLM and still very simple but is a one shot approach as only one firing is available. Some technologies with membrane to stop the combustion and opens the possibility to fire multiple times might be an option but is out of the scope of this paper.

### 6.2 Conclusion

The presented results give interesting insights regarding the different performances of the four micro-engines and their most correct ranges of applicability. In general, we can see the Liquid Vapour propellant as an improved version of the Cold Gas thruster in terms of specific impulse and of tank volume needed in total, at the price of a much higher

requested power. On the other hand, the bipropellant has the best specific impulse of all and the smallest tanks, but it comes with much more complex and non-optimized systems for MEMS propulsion. The Solid Rocket Motors is a simple system with good performance, with negligible requested power. Despite this, SRMs have the major drawback of being non-restartable, non-thrutable and one-shot systems. The thrust coefficients are pretty close for all the systems, as they represent only the performance of the nozzles, which are very similar one to another.

To sum up, each of the four systems have its own range of usage and is most properly implementable for different kinds of missions. The solid propulsion is one of the best in terms of performances, but implementable just in missions without strict requirements in terms of thrust control. Future development may include the grain section manipulation with different shapes and further advances in the mixing techniques.

Cold gas thrusters are the simplest system, with the highest heritage in the MEMs propulsion, as mentioned in Sec. 1.2.3. This makes them the safest to use, but implementable just for a mission where low performance is allowed. Future developments may include improvement in FLM drilling to produce axialsymmetric nozzles with more accurate alignment, or implementation of liquid propellant as the R236fa for improved performance and smaller tanks.

Vapor Liquid motors are mainly compliant with attitude propulsion, because of their particular easiness to switch on and off, with increased performances with respect to cold gas thruster, investing some of the electric power. Furthermore, they can be particularly useful in dissipating on-board electronics heat, instead of using dedicated power. Future developments can regard the redesign of the nozzle, increasing the expansion ratio and therefore the efficiency.

The bipropellant is a promising technology for future applications of the MEMS propulsion with its higher performance, however by now its miniaturization is still a challenge. Just as for bigger satellites, bipropellant could be more adapt for bigger burns, so for orbital manoeuvres.

## References

- [1] L Mele, F Santagata, E Iervolino, M Mihailovic, T Rossi, AT Tran, H Schellevis, JF Creemer, and PM Sarro. A molybdenum mems microhotplate for high-temperature operation. *Sensors and Actuators A: Physical*, 188:173–180, 2012.
- [2] Marc J. Madou. *Foundamentals of Microfabrication and Nanotechnology*. Taylor Francis Group, 2011.
- [3] Archived on 9 April 2025.
- [4] Kean How Cheah and Kay-Soon Low. Fabrication and performance evaluation of a high temperature co-fired ceramic vaporizing liquid microthruster. *Journal of Micromechanics and Microengineering*, 2015.
- [5] K. Karthikeyan, S.K. Chou, L.E. Khoong, Y.M. Tan, C.W. Lu, and W.M. Yang. Low temperature co-fired ceramic vaporizing liquid microthruster for microspacecraft applications. *Applied Energy*, 97:577–583, 2012. Energy Solutions for a Sustainable World - Proceedings of the Third International Conference on Applied Energy, May 16-18, 2011 - Perugia, Italy.
- [6] Kean How Cheah, Chaggai Ganani, Kristina Lemmer, and Angelo Cervone. Chapter 2 - cold gas microthruster. In Kean How Cheah, editor, *Space Micropulsion for Nanosatellites*, pages 23–50. Elsevier, 2022.
- [7] London A. P. *DEVELOPMENT AND TEST OF A MICROFABRICATED BIPROPELLANT ROCKET ENGINE*. PhD thesis, Massachusetts Institute of Technology, 2000.
- [8] M Louwerse, H.V. Jansen, M Groenendijk, and M. Elwenspoek. Nozzle fabrication for micropulsion of a microsatellite. *Journal of Micromechanics and Microengineering*, 19:045008, 03 2009.
- [9] Huichao Li, Yukui Wang, Zhenlong Wang, and Zhaoxi Zhao. Fabrication of zrb2-sic-graphite ceramic micro-nozzle by micro-edm segmented milling. *Journal of Micromechanics and Microengineering*, 28:105022, 08 2018.
- [10] Xuhui Liu, Teng Li, Zhoubo Li, Hongpeng Ma, and Shuzhou Fang. Design, fabrication and test of a solid propellant microthruster array by conventional precision machining. *Sensors and Actuators A: Physical*, 236:214–227, 2015.
- [11] David H Lewis Jr, Siegfried W Janson, Ronald B Cohen, and Erik K Antonsson. Digital micropulsion. *Sensors and Actuators A: Physical*, 80(2):143–154, 2000.
- [12] Silva MC Guerrieri DC. Selection and characterization of green propellants for micro-resistojets. *ASME Journal of Heat Transfer*, 2017.
- [13] R. H. Lee, A. M. Bauer, M. D. Killingsworth, T. C. Lilly, J. A. Duncan, and A. D. Ketsdever. Free-molecule-microresistojet performance using water propellant for nanosatellite applications. *Journal of Spacecraft and Rockets*, 45(2):264–269, 2008.
- [14] Kristoffer Palmer, Hugo Nguyen, and Greger Thornell. Fabrication and evaluation of a free molecule microresistojet with thick silicon dioxide insulation and suspension. *Journal of Micromechanics and Microengineering*, 23(6):065006, apr 2013.
- [15] Archive April 9 2025.
- [16] Kamlesh D. Patel, Michael S. Bartsch, Matthew H. McCrink, Jennifer S. Olsen, Bruce P. Mosier, and Robert W. Crocker. Electrokinetic pumping of liquid propellants for small satellite microthruster applications. *Sensors and Actuators B: Chemical*, 132(2):461–470, 2008. Transducers '07/Eurosensors XXI.
- [17] Pijus Kundu, Arun Kumar Sinha, Tarun K. Bhattacharyya, and Soumen Das. MnO<sub>2</sub> nanowire embedded hydrogen peroxide monopropellant mems thruster. *Journal of Microelectromechanical Systems*, 22(2):406 – 417, 2013. Cited by: 27.
- [18] Al Midani O. M. *Preliminary Design of a Liquid Bipropellant Microfabricated Rocket Engine*. PhD thesis, Massachusetts Institute of Technology, 1998.
- [19] Christopher S. Protz. *Experimental Investigation of MicroFabricated Bipropellant Rocket Engines*. PhD thesis, Massachusetts Institute of Technology, 2004.

- [20] Yubin Zhong, Fabrizio liquid, Francesco Barato, Guojun Xia, Siyu Li, Xiao Zhang, and Tao Wu. Design and analysis of a micro-electro-mechanical system thruster for small satellites and low-thrust propulsion. *Aerospace*, 12(3), 2025.
- [21] Logan Williams, Michael McDonald, and Michael Osborn. Performance characterization of a low reynolds number micro-nozzle flo. In *AIAA Propulsion and Energy Forum*, 07 2015.
- [22] E Parra, Kristofer Pister, and C Fernandez-Pello. Solid-propellant micro-thruster. 01 2006.
- [23] Luigi DeLuca, Filippo Maggi, Stefano Dossi, Volker Weiser, Andrea Franzin, and Volker Gettwert. High-energy metal fuels for rocket propulsion:characterization and performance. *Huo zhaya o Xuebao/Chinese Journal of Explosives and Propellants*, 2013:1–14, 12 2013.
- [24] Xuhui Liu, Teng Li, Zhoubo Li, Hongpeng Ma, and Shuzhou Fang. Design, fabrication and test of a solid propellant microthruster array by conventional precision machining. *Sensors and Actuators A: Physical*, 236:214–227, 2015.
- [25] Kaili Zhang, S.K. Chou, and S.S. Ang. Mems-based solid propellant microthruster design, simulation, fabrication, and testing. *Journal of Microelectromechanical Systems*, 13(2):165–175, 2004.
- [26] Xinjie Li, Guobiao Cai, Junya Yuan, Yatao Chen, Bijiao He, and Lihui Liu. Influences of geometry configurations on the performance of micro-nozzles. *Acta Astronautica*, 215:618–630, 2024.
- [27] Jianbing Xu, Jiangtao Zhang, Fuwei Li, Shiyi Liu, Yinghua Ye, and Ruiqi Shen. A review on solid propellant micro-thruster array based on mems technology. *FirePhysChem*, 4(2):95–106, 2024. Micromotors and Other Special Topics in Propulsion.
- [28] Jeongrak Lee, Seonghyeon Kim, Hanseong Jo, Eunji Lee, and Anna Lee. Design and fabrication of a scalable solid-propellant micro-thruster array using lab-on-pcb technology. *Sensors and Actuators A: Physical*, 363:114738, 2023.
- [29] Fahid Riaz Ravi Ranjan, S. K. Chou and Kumarasamy Karthikeyan. Cold gas micro propulsion development for satellite application. *Energy Procedia*, 143:754–761, 2017.
- [30] Crane Co. *Flow of fluids through valves, fittings, and pipe*. Number 410. Crane Company, 1988.
- [31] Travis K Imken, Terry H Stevenson, and E Glenn Lightsey. Design and testing of a cold gas thruster for an interplanetary cubesat mission. *Journal of Small Satellites*, 4(2):371–386, 2015.
- [32] J.W. Cen and J.L. Xu. Performance evaluation and flow visualization of a mems based vaporizing liquid micro-thruster. *Acta Astronautica* 67, 2010.
- [33] EV Mukerjee, AP Wallace, KY Yan, DW Howard, RL Smith, and SD Collins. Vaporizing liquid microthruster. *Sensors and Actuators A: Physical*, 83(1-3):231–236, 2000.
- [34] ThermExcel. Water - thermodynamic properties, 2025. Accessed: April 9, 2025.
- [35] OSEPH J. M A R T I N and JOHN B. EDWARDS. *Correlation of Latent Heats of Vaporization*. The University of Michigan, Ann Arbor, Michigan, 1965.
- [36] Y. Z. Zhang. Thermophysical interpretation of the latent heat of vaporization of water. *International Journal of Thermophysics*, 1989.
- [37] DONALD F. OTHMER. *Correlating Vapor Pressure and Latent Heat Data A NEW PLOT*. Polytechnic Institute of Brooklyn, Brooklyn, N. Y., 1940.
- [38] Emmanuel Tatakos Michael Loupis John Spanoudakis John Karatzafaris, Nick Papanikolaou. *Fundamentals of Heat and Mass Transfer*. JOHN WILEY SONS, 2007.
- [39] A Cervone, B Zandbergen, D Cordeiro Guerrieri, M De Athayde Costa e Silva, I Krusharev, and H Van Zeijl. Green micro-resistojet research at delft university of technology: new options for cubesat propulsion. *CEAS Space Journal*, 9:111–125, 2017.
- [40] Ignoto Ignazzo. Diagrammi e tavole. Technical report, DIPARTIMENTO DI TERMOENERGETICA E CONDIZIONAMENTO AMBIENTALE, Università di Genova, 2000.

- [41] Yasuhiro Kawakatsu, Kiyoshi Kuramoto, Tomohiro Usui, Haruna Sugahara, Hisashi Ootake, Ryoichiro Yasumitsu, Kent Yoshikawa, Stephane Mary, Markus Grebenstein, Hirotaka Sawada, et al. Preliminary design of martian moons exploration (mmx). *Acta Astronautica*, 202:715–728, 2023.
- [42] Flippo Maggi. Tables extract quasi 1d flow. [https://webeep.polimi.it/pluginfile.php/1334412/mod\\_folder/content/0/Tables-extract-quasi1Dflow.pdf?forcedownload=1](https://webeep.polimi.it/pluginfile.php/1334412/mod_folder/content/0/Tables-extract-quasi1Dflow.pdf?forcedownload=1), 2025. Accessed: 2025-04-09.
- [43] G.P. Sutton and O. Biblarz. *Rocket Propulsion Elements, Ninth Edition*. John Wiley & Sons (US), 2017.
- [44] J.K. Chin K.H. Cheah. Performance improvement on mems micropropulsion system through a novel two-depth micronozzle design. *Acta Astronautica*, 2011.
- [45] M. Athayde Costa e Silva. *MEMS Micropropulsion Design, Modeling and Control of Vaporizing Liquid Microthrusters*. PhD thesis, Delft, 2018.
- [46] Dieter K. Huzel and David H. H liang. Design of liquid propellant rocket engines. Technical report, NASA, 1967.
- [47] M. L.L. Ianuzzi, J. M. Hollingshead, A. C. Risha, Jeffrey David Moore, and G. A. Risha. Effect of impingement angle on flame stability in a non-premixed methane/oxygen diffusion flame burner. *Combustion science and technology*, 2024. Publisher Copyright: © 2024 Taylor Francis Group, LLC.
- [48] Sebastian Gnagy Stavros Diamantopoulous Amelia Greig Peter Van Ness, Geraldo Ramirez Jr. Pressurized 1u cubesat propulsion unit. *AIAA/USU Conference on Small Satellites*, 2019.
- [49] Xue'en Yang. A mems valve for the mit microengine. 2001.
- [50] A.M. Cardenas-Valencia, J. Dlutowski, J. Bumgarner, C. Munoz, W. Wang, R. Popuri, and L. Langebrake. Development of various designs of low-power, mems valves for fluidic applications. *Sensors and Actuators A: Physical*, 136(1):374–384, 2007. 25th Anniversary of Sensors and Actuators A: Physical.

## A Authorship Declaration

### AUTORSHIP DECLARATION

	LITERATURE	MODELING	CODING
<b>Bacconier Marc</b>	-Cold-gas	-Cold-gas	-Cold-gas design
<b>Carminati Matteo</b>	-Cold-gas	-Cold-gas	-Cold-gas design -Cold-gas Monte Carlo
<b>Chianese Elena Maria</b>	-Bipropellant -Solid propellant -Micronozzles -Uncertainties	-Solid propellant -Bipropellant	-Solid propellant design -Bipropellant design
<b>Cocomazzi Marco</b>	-Liquid Vapor Thermodynamics -Liquid Vapor Architecture	-Liquid vapor	-Liquid vapor design
<b>Colombo Andrea</b>	-Cold-gas	-Cold gas	-Cold-gas design -Cold-gas Monte Carlo -Bipropellant Monte Carlo
<b>Coppola Riccardo</b>	-Solid Propellant	-Solid Propellant	-Solid propellant design -Solid propellant Monte Carlo
<b>Corbo Nicolò</b>	-Liquid vapor Thermodynamics -Liquid vapor Architecture	-Liquid Vapor	-Liquid vapor Design -Liquid vapor Montecarlo
<b>Donati Filippo</b>	-Bi-propellant -Thermodynamics -Liquid Vapor -MEMs materials -MEMs state of art		-Bipropellant Monte Carlo
<b>Pezzi Francesco</b>	-Solid propellant -Bipropellant	-Solid propellant -Bipropellant	-Solid propellant design -Bipropellant design -Solid propellant Monte Carlo